Controls on boron isotopes in a cold-water coral and the cost of resilience to ocean acidification

Alexander C. Gagnon[1*], Anne M. Gothmann[1,2,3], Oscar Branson[4], James W. B. Rae[5], and Joseph A. Stewart[6]

[1]School of Oceanography, University of Washington, Seattle, WA, USA.
[2]Joint Institute for the Study of the Atmosphere and Ocean, University of Washington, Seattle, WA, USA.
[3]Departments of Physics and Environmental Studies, St. Olaf College, Northfield, MN, USA.
[4]Department of Earth Sciences, University of Cambridge, Cambridge, UK.
[5]School of Earth and Environmental Science, University of St. Andrews, St. Andrews, UK.
[6]School of Earth Sciences, University of Bristol, Bristol, UK.
*email: gagnon@uw.edu

Coral skeletal growth is sensitive to environmental change and may be adversely impacted by an acidifying ocean. However, physiological processes can also buffer biomineralization from external conditions, providing apparent resilience to acidification in some species. These same physiological processes affect skeletal composition and can impact paleoenvironmental proxies. Understanding the mechanisms of coral calcification is thus crucial for predicting the vulnerability of different corals to ocean acidification and for accurately interpreting coral-based climate records. Here, using boron isotope ($\delta^{11}B$) measurements on cultured cold-water corals, we explain fundamental features of coral calcification and its sensitivity to environmental change. Boron isotopes are one of the most widely used proxies for past seawater pH, and we observe the expected sensitivity between $\delta^{11}B$ and pH. Surprisingly, we also discover that coral $\delta^{11}B$ is independently sensitive to seawater dissolved inorganic carbon (DIC). We can explain this new DIC effect if we introduce boric acid diffusion across cell membranes as a new flux within a geochemical model of biomineralization. This model independently predicts the sensitivity of the $\delta^{11}B$-pH proxy, without being trained to these data, even though calcifying fluid pH (pH_{CF}) is constant. Boric acid diffusion resolves why $\delta^{11}B$ is a useful proxy across a range of calcifiers, including foraminifera, even when calcifying fluid pH differs from seawater. Our modeling shows that $\delta^{11}B$ cannot be interpreted unequivocally as a direct tracer of pH_{CF}. Constant pH_{CF} implies similar calcification rates as seawater pH decreases, which can explain the resilience of some corals to ocean acidification. However, we show that this resilience has a hidden energetic cost such that calcification becomes less efficient in an acidifying ocean.

Keywords: boron isotopes; coral; biomineralization; ocean acidification; pH proxy; B/Ca

1. Introduction

Tropical and cold-water coral reefs, which are exceptionally diverse and valuable marine ecosystems, are built through the process of skeletal calcification. Ocean acidification (OA) can slow calcification, with more than half of tropical reefs predicted to enter a state of net dissolution and decline by midcentury (Pandolfi et al., 2011). This sensitivity to environmental conditions exists even though calcification occurs within an extracellular fluid that is partially separated from and modified with respect to ambient seawater (Allemand et al., 2004). Indeed, corals elevate the pH of this calcifying fluid (pH_{CF}) with respect to seawater (Al-Horani et al., 2003; McColloch et al, 2012a; Venn et al., 2013; Cai et al., 2016), likely through Ca^{2+}-$2H^{+}$ exchange or other alkalinity pumps (McConnaughey 1989; Zoccola et al., 2004). This pH elevation can enhance the thermodynamic driving force for skeletal growth and can moderate some of the effects of OA, but active pumping requires energy. Mapping the sensitivity of pH_{CF} to external conditions and measuring the cost of this buffering are crucial targets for understanding the resilience of coral calcification in a changing ocean and for interpreting pH paleoproxies.

Boron isotope ratios ($\delta^{11}B = (({}^{11}B/{}^{10}B)/({}^{11}B/{}^{10}B)_{standard} - 1)*1000$; referenced to standard NIST SRM 951) are increasingly used to infer pH_{CF} in coral (for example, McCulloch et al., 2017; Nicola et al., 2018; Comeau et al., 2019; Giri et al., 2019). The $\delta^{11}B$ of aragonite, the skeletal $CaCO_3$ mineral used by both cold-water and tropical stony (scleractinian) corals, is sensitive to the pH of the surrounding fluid. This is because aragonite selectively co-precipitates borate ion (Noireaux et al., 2015) and the $\delta^{11}B$ of this dissolved borate ion changes with pH, relative to total

boron (Hemming and Hanson, 1992; Branson, 2018). When the $\delta^{11}B$ of total boron in the calcifying fluid is the same as seawater, then skeletal $\delta^{11}B$ should indicate pH_{CF}. Through an implicit assumption about the link between pH_{CF} and seawater pH, the $\delta^{11}B$ of ancient coral skeletons and other marine calcifiers is also used to infer past ocean pH (Hemming and Hönisch, 2007).

The acid-base chemistry of seawater, which is primarily controlled by the equilibrium between different species of dissolved inorganic carbon, is not only a function of pH but instead has two degrees of freedom. As a result, one carbonate system parameter can be held constant (e.g. pH) while the values of the other parameters (e.g., DIC, CO_3^{2-}, alkalinity, HCO_3^-, pCO_2) change in unison. This flexibility paves the way for experiments that can test which carbonate system parameters are most responsible for the physiological and geochemical response of marine calcifiers to ocean acidification (Schneider and Erez, 2006; Waldbusser et al., 2015). For example, when the tropical coral *Stylophora pistillata* is cultured at constant seawater pH, pH-sensitive dyes show that pH_{CF} still varies, and does so systematically with other seawater carbonate system parameters (Comeau et al., 2016). These data suggest a complicated dependency between seawater chemistry and pH_{CF}, which could cause coral calcification to respond to different environmental conditions in counterintuitive ways. Furthermore, if pH_{CF} sets skeletal $\delta^{11}B$, then $\delta^{11}B$ records may be sensitive to carbonate system parameters other than just seawater pH.

To resolve the impact of individual carbonate system parameters on $\delta^{11}B$, we cultured the cold-water coral *Balanophyllia elegans* at constant temperature, but

across 13 different static carbonate chemistry conditions divided into three groups, with either pH, carbonate ion, or DIC kept constant. *B. elegans* was chosen as a simple model of biocalcification because, like many cold-water corals, it lacks photosymbionts. The $\delta^{11}B$ of cold-water corals is also increasingly used to infer past changes in seawater pH and the marine carbon cycle (Rae et al., 2018). Furthermore, several experiments with cold-water corals show unexpected resilience to OA (McCulloch et al., 2012b; Crook et al., 2013; Rodolfo-Metalpa et al., 2015). While this resilience is commonly attributed to up-regulation of calcifying fluid pH (McCulloch et al., 2012a), the energetic cost of this strategy and its sensitivity to environmental factors remain poorly understood. Our experiments test whether seawater pH is the primary control on skeletal $\delta^{11}B$ in a cold-water coral and, together with a geochemical model of coral biomineralization, elucidate mechanisms that govern how coral calcification responds to seawater chemistry.

2. Materials and Methods

2.1 Coral culture

The genus *Balanophyllia* is a cosmopolitan stony coral that is found globally and at depths from the intertidal to several thousand meters. Fossil specimens have been used to reconstruct seawater chemistry back to the Eocene (Gothmann et al., 2015). The species cultured in this study (*Balanophyllia elegans)* is a cold-water coral found on the West Coast of the United States from Alaska to Baja California and from intertidal to 500 m (Durham and Barnard, 1952; Gerrodette, 1979). Living *B. elegans*

adults, including gravid females, were collected by divers from a depth of 15-22m near Friday Harbor Labs, San Juan Island, Washington, USA. Collections were conducted early in the planulation season (late December) so that there was a higher likelihood of recovering planulae from adults. Ambient pH at this location varies from 7.6 to 8.0, with an average value of 7.8 (Murray et al., 2015). Adult corals were allowed to recover in sea tables lined with 3-by-1-inch glass microscope slides to provide a recruitment surface for *B. elegans* planulae. Planulae appeared in the tank on the same day adults were collected, and 135 larvae settled and metamorphosed within two and a half weeks. After settlement, coral larvae were randomly assigned to 13 different culture conditions. For each culture condition, there were approximately 9 individuals divided into 3 separate trace metal clean plastic culture vessels. These culture vessels were maintained at a constant temperature of 10.95 +/- 0.43 °C (2 S.D.) for ~100 days. Seawater with a typical salinity of 28.4, sourced from Puget Sound at the NOAA Mukilteo Research Station and filtered to 1µm, was used to replace the culture solution every ~3.5 days. Corals were transferred between two sets of culture vessels during water changes to minimize handling time. Prior to each water change, new seawater was brought to culture temperature and the alkalinity and DIC of each replacement culture vessel was adjusted using $NaHCO_3$ together with HCl or NaOH to match the respective targets listed in Table 1. Culture vessels had no headspace, were sealed with parafilm, and then capped to limit gas exchange. Feeding with *Artemia salina* nauplii was conducted every ~7 days during water changes. Regular analysis of alkalinity and DIC, of both initial and post water change culture solutions, confirm that

carbonate system conditions were maintained within narrow bounds during the time between seawater exchanges and across different bottles during the duration of the experiment. Dissolved inorganic carbon was measured using a coulometer (UIC, Inc.) coupled to a dissolved inorganic carbon acidification unit (VINDTA, MIRANDA). Alkalinity was measured using a custom titration system with a low noise amplifier (built by Andrew Dickson, SIO). Both techniques were standardized against a certified reference material (Andrew Dickson, SIO). The long-term reproducibility of regularly measured standards using these techniques is +/- 3.2 μmoles kg^{-1} for DIC and +/- 4.8 μmoles kg^{-1} for alkalinity (2 S.D. over 2 years).

2.2 Overall skeletal growth

At the end of the ~100 days, cultured corals were sacrificed, rinsed, cleaned with bleach, rinsed again, dried, separated from their slides, and weighed using a Sartorius Cubis MSA6.6S0TRDM microbalance. Final skeletal mass ranged from 0.5 to 2.5 mg. Skeletal mass increased with culture water DIC following a significant (*p*-value = 0.00015) but scattered (R^2 = 0.18) linear relationship (Fig. 1). The slope of this relationship (0.21 ± 0.05 mg $mmol^{-1}$ kg) implies a 38 % change in average skeletal mass across the 3 mmol kg^{-1} of DIC explored in the culture experiments. Despite experiments in oysters (Waldbusser et al., 2015) and tropical corals (Schneider and Erez, 2006) showing a relationship between calcification rates and $CaCO_3$ saturation state, final skeletal mass in *B. elegans* did not follow a significant linear relationship with either carbonate ion concentration or pH. Note that carbonate ion concentration and saturation state covary in our experiments because

calcium concentrations are similar across all experiments. The saturation state (Ω) = $[CO_3^{2-}][Ca^{2+}]/K_{sp}$, where K_{sp} is the equilibrium solubility product of aragonite, the $CaCO_3$ polymorph that scleractinian corals use for their skeletons.

2.3 Geochemical analysis

Skeletal subsamples of 150 to 500 µg were analyzed for $\delta^{11}B$ and B/Ca. Because sample size was small, no precleaning beyond the initial bleaching of the whole specimen was applied. Samples were dissolved in distilled 0.5 M HNO_3. An aliquot of the dissolved sample was analyzed by Inductively Coupled Plasma-Mass Spectrometry (ICP-MS) at Univ. of Bristol using well-characterized, matrix-matched, synthetic standard solutions to yield B/Ca ratios. Repeat analysis of NIST RM 8301c (n=35) yielded analytical precision of ± 2% (2SD).

A further aliquot of the dissolved sample containing ~40 ng B was separated from the carbonate matrix using 20 µl micro-columns containing Amberlite IRA 743 boron-specific anionic exchange resin (Kiss, 1988; Foster, 2008). The $\delta^{11}B$ of purified boron samples were measured by Multi Collector-ICP-MS (Neptune Plus, Thermo) against NIST SRM 951 at Univ. of St Andrews following Foster (2008), but with samples, blanks, and standards introduced to the instrument in a 0.5 M HNO_3 and 0.3 M HF acid matrix to aid B wash out (Misra et al., 2014; Rae et al., 2018). Total procedural blanks (n=4) had an average $\delta^{11}B$ of 39.5‰ and were all <0.8% of sample boron, thus blank corrections were small (<0.08‰). Full procedural uncertainty is assessed using repeat measurement of NIST 8301c consistency

standard run during this analytical campaign, yielding an average $\delta^{11}B$ value of 24.15± 0.14‰ (2SD, n=4) that is consistent with long term lab reproducibility. Skeletal data are summarized in Table 2.

2.4 Initial skeletal material

A small amount of skeletal growth occurred between settlement and placement into treatment conditions. Apart from this initial material, all skeletal mass grew under specific and controlled conditions. Several corals were sacrificed at the beginning of the experiment to estimate the amount of initial material. Using X-ray computed tomography we estimate that initial skeletal material is about ~0.05 mm^3, which would correspond to a mass of ~0.14 mg assuming the initial coral has a density typical of aragonite (2.93 g/cm^3). The initial material represents 6-23% of final skeletal mass. On average, this represents a systematically smaller part of skeletons as seawater DIC increases because of trends in skeletal mass. If the initial skeleton has a distinct $\delta^{11}B$ signature, then more or less growth as a function of DIC could result in an apparent DIC effect that is actually driven by mixing. This mixing effect would be evident as a relationship between $\delta^{11}B$ and final sample mass.

We tested our dataset for this mixing relationship and found that mixing cannot explain the systematic relationships we see between $\delta^{11}B$ and DIC, pH, or $[CO_3^{2-}]$, as described below. The primary evidence for a $\delta^{11}B$ DIC effect comes from the constant pH experiments described below. However, there is no significant relationship between sample mass and $\delta^{11}B$ for this experiment (Supplemental Fig.

1). There is no relationship between $\delta^{11}B$ and sample mass for the constant carbonate ion experiment either. For the constant DIC experiment there is a weak relationship between $\delta^{11}B$ and skeletal mass, but this is consistent with a similarly weak covariance between pH and skeletal mass in the subset of coral randomly chosen for $\delta^{11}B$ analysis. Thus, the strong $\delta^{11}B$ -pH effect in our coral cannot be explained by mixing. A similar analysis for skeletal B/Ca shows that mixing cannot explain the B/Ca vs. DIC effect in the constant pH and constant [CO_3^{2-}] experiments (Supplemental Fig. 2).

2.5 Impact of transmembrane boric acid diffusion on skeletal $\delta^{11}B$

A simple analytical model of the calcifying fluid is sufficient to describe the impact of boric acid diffusion on skeletal $\delta^{11}B$. This analytical approach was used to generate Figure 5. In contrast to the full numerical model described below, only diffusion and seawater exchange are considered in this analytical model. This is because co-precipitation of boron into skeletal aragonite is typically a small flux compared to the large concentration of boron in seawater. Furthermore, carbonate chemistry is not needed in this simple model. This is because we are investigating the sensitivity of $\delta^{11}B$ to specified pH_{CF} and seawater pH values rather than calculating pH values as a function of calcification physiology, as is done in the full model. The governing differential equations for this simple model are:

$$\begin{aligned} \frac{d[\mathrm{B_T}]}{dt} = \quad & k[\mathrm{B_T}]_{sw} - k[\mathrm{B_T}] && \text{seawater exchange} \\ & + \frac{D}{z}\frac{1}{\beta}[\mathrm{B(OH)_3}]_{ext} - \frac{D}{z}\frac{1}{\beta}\chi_B[\mathrm{B_T}] && \mathrm{B(OH)_3\ diffusion} \end{aligned}$$

$$\frac{d[^{11}\mathrm{B_T}]}{dt} = k[\mathrm{B_T}]_{sw}{}^{11}A_{Tsw} - k[\mathrm{B_T}]^{11}A_T \quad \text{seawater exchange}$$
$$+ \frac{D}{z}\frac{1}{\beta}[\mathrm{B(OH)_3}]_{ext}{}^{11}A_{B3sw} - \frac{D}{z}\frac{1}{\beta}\chi_B[\mathrm{B_T}]^{11}A_{B3} \quad \mathrm{B(OH)_3}\ \text{diffusion}$$

230

231

232 which reduce to the following system of equations at steady-state:

233

$$0 = [\mathrm{B_T}]_{sw} - [\mathrm{B_T}] + \frac{D}{kz}\frac{1}{\beta}[\mathrm{B(OH)_3}]_{ext} - \frac{D}{kz}\frac{1}{\beta}\chi_B[\mathrm{B_T}]$$

234

235 and

236

$$0 = [\mathrm{B_T}]_{sw}{}^{11}A_{Tsw} - [\mathrm{B_T}]^{11}A_T + \frac{D}{kz}\frac{1}{\beta}[\mathrm{B(OH)_3}]_{ext}{}^{11}A_{B3sw} - \frac{D}{kz}\frac{1}{\beta}\chi_B[\mathrm{B_T}]^{11}A_{B3}$$

237

238

239 The non-dimensional variable *D/kz* represents the balance between diffusion and
240 seawater exchange. The variable β, which indicates the ratio of diffusion for $CO_{2(aq)}$
241 compared to $B(OH)_3$, allows *D/kz* to control diffusion for both species. The variable
242 β is set to 1 in this simple model because there is no carbonate system, but it can be
243 varied to other values in the full model described below. The variable χ_B represents
244 the pH_{CF} dependent mole fraction of total boron (B_T) that is boric acid. Boron-11
245 abundances of different species or reservoirs are indicated as ^{11}A. Skeletal $\delta^{11}B$ is
246 assumed to match the $\delta^{11}B$ of calcifying fluid borate, which is calculated from $[^{11}B_T]$
247 subject to an equilibrium isotope fractionation between boric acid and borate of
248 1.0272 (Klochko et al., 2006), mass balance, and pH_{CF}.

249

2.6 Geochemical model of coral biomineralization

Our steady-state equilibrium approach is described in detail together with model-data comparisons in Supplemental Information 2: *Geochemical model of coral biomineralization*. The coral skeleton grows from a calcifying microenvironment that is modeled as a single box of modified seawater called the calcifying fluid (Fig. 2). Calcifying fluid chemistry can be modified through a host of physiological and geochemical processes. While a large number of processes could be considered, we attempted to find the simplest general model that can reproduce our data and make useful predictions. We then show that it is unnecessary to know specific fluxes. Instead we show that skeletal chemistry is primarily controlled by just three low dimension parameters. To interpret the significance of these parameters and to explain the structure of the model, we start by defining individual fluxes. The model includes fluxes due to skeletal precipitation P in moles $CaCO_3$ m^{-2} sec^{-1}; seawater exchange (k) in sec^{-1}, where k is just the inverse of the calcifying fluid residence time; and diffusion of the two nonpolar species $CO_{2(aq)}$ and $B(OH)_3$.

One major difference between this and other models is the consideration of boric acid diffusion. Diffusion D of a species across the cell membrane is put in terms of a piston velocity in units of m sec^{-1}. This piston velocity simply represents the diffusion coefficient in m^2 sec^{-1} multiplied by a cell membrane thickness. The piston velocity D is specific to $CO_{2(aq)}$ diffusion. To account for differences between $CO_{2(aq)}$ and $B(OH)_3$ diffusion we define the parameter β, such that the piston velocity for $B(OH)_3$ is D/β.

The model also includes active ion pumping by the coral organism. To keep the model as general as possible, this flux is treated as alkalinity pumping F in units of 2x mole equivalents m^{-2} sec^{-1}. This is equivalent to Ca^{2+}-$2H^{+}$ exchange. Other stoichiometries are equivalent from the perspective of the main governing equations of the model, including $2Na^{+}$-$2H^{+}$ or $2K^{+}$-$2H^{+}$ exchanges. The only impact of these different modes of ion pumping would be on $[Ca^{2+}]$ but this term is not necessary to determine the B/Ca or $\delta^{11}B$ composition of the skeleton in our model. As part of the model, we introduce the term $\gamma = F/P$. This non-dimensional parameter has physiological significance because it represents the amount of active ion pumping relative to the amount of precipitation; therefore it is a measure of calcification efficiency.

The carbonate species of the calcifying fluid are assumed to be in equilibrium with each other as are the two dissolved boron species. Kinetic effects are most relevant for isotopes systems other than those considered this study, like $\delta^{18}O$, where reaction hydration/hydroxylation can slow isotopic exchange (McConnaughey, 1989; Chen et al., 2018). Furthermore, the indirect impacts of disequilibrium due to slow hydration/hydroxylation could result in a partial decoupling of $CO_{2(aq)}$ from DIC, which would likely only result in minor pH offsets from our equilibrium results and manifest as an apparently slower diffusion coefficient for this species. As these effects of hydration/hydroxylation kinetics are not expected to change the main

patterns or conclusions of our current study, we assume chemical equilibrium and we will consider the impact of kinetics on boron in future work.

Skeletal $\delta^{11}B$ is assumed to match the $\delta^{11}B$ of calcifying fluid borate (Noireaux et al., 2015), which is calculated subject to an equilibrium isotope fractionation between boric acid and borate of 1.0272 (Klochko et al., 2006), mass balance, and pH_{CF}. With regards to the relationship between skeletal B/Ca and calcifying fluid chemistry, inorganic aragonite coprecipiation experiments do not show the strong kinetic effects of calcite (Farmer et al., 2019) and are instead consistent with two different simple forms of the partition coefficient described by Holcomb et al (2016). We use the two partition coefficients from Holcomb et al. that best fit their inorganic precipitation data. The first form is in terms of [B]/DIC:

$$B/Ca_{skeleton} = 2.88\times10^{-3}\ [B]_{CF}/DIC_{CF} + 8.5\times10^{-5} \quad \text{(in mol/mol)}$$

The implementation of the model is modular and can accommodate different transfer functions. For example, setting the partition coefficient in terms of $[B(OH)_4^-]/\sqrt{[CO_3^{2-}]}$, as also described in Holcomb et al., shifts the modeled B/Ca to slightly higher values, but does not alter the trends nor does it change the main conclusions of our paper.

As described in Supplemental Material 2, the governing differential equations for the calcifying fluid can be solved for steady-state solutions and are only a function of pH_{CF}, D/kz, and $P/kz\rho$. The variable $P/kz\rho$ represents the balance between precipitation and seawater exchange. It is in units of concentration (mol kg^{-1}), it

equals the steady state draw down of alkalinity or calcium, and it acts as an indicator for the extent of Rayleigh fractionation. One advantage of our modeling framework is that it is agnostic about the relative importance of active ion pumping, seawater exchange, and Rayleigh processes. Biomineralization models from the literature that emphasize these different processes just correspond to different regions in 3-dimensional model space. Only the data from the constant pH experiment are used to tune these parameters. The calcifying fluid pH is assumed to be constant for all coral. The tuned value of pH_{CF} and $P/kz\rho$ as well as the dependence of D/kz on seawater DIC are then applied to the other two independent experiments without additional tuning. Different results between the experiments are therefore ultimately a function of seawater chemistry, but this behavior is set by general rules.

Alternatively, an inorganic rate law for aragonite mineral growth can be included in the model: $P = k(\Omega\text{-}1)^n$; where the constants k and n are fit to previous inorganic experiments, and Ω is the aragonite saturation state of the calcifying fluid. The resulting precipitation rate (P) is then used to decompose the dynamical parameters $P/kz\rho$ and D/kz into component fluxes. In this case, a single value for D/β rather than $P/kz\rho$ is tuned to the data. As before, only the data from the constant pH experiment are used for tuning. The single value of pH_{CF}, as well as the dependence of D/kz on seawater DIC are tuned as before. These parameters are then applied to the other two independent experiments without additional tuning. Both approaches yield similar results as far as $\delta^{11}B$, B/Ca, and calcifying fluid chemistry because pH_{CF}, D/kz , and $P/kz\rho$ control these quantities. The main difference between the two

approaches is the implied value of D/β. The parameter D/β varies in the first approach but is constant in the later approach, where $P/kz\rho$ is then allowed to change as a function of seawater DIC but without tuning.

3. Results and Discussion

3.1 Both seawater DIC and pH affect skeletal $\delta^{11}B$ in cold-water corals

If seawater pH were the sole control on skeletal $\delta^{11}B$, then $\delta^{11}B$ should remain unchanged when cold-water corals are cultured at constant pH. We instead find a systematic decrease in $\delta^{11}B$ of –1.08 ‰ per mmol/kg change in DIC (Fig. 3a). Across the range of DIC in the modern ocean, which is approximately 400 μmol kg^{-1} (Olsen et al., 2016), this DIC effect would result in a pH error of 0.1 if it were conventionally interpreted as a pH effect. Additional evidence for the influence of DIC comes from our constant $[CO_3^{2-}]$ and constant DIC experiments. In both experiments pH has a clear effect, but $\delta^{11}B$ is 2.5 times more sensitive to pH in the constant $[CO_3^{2-}]$ experiment (Fig. 3b, Supplementary Fig. 7). This difference is driven by the co-variation of both pH and DIC in the constant $[CO_3^{2-}]$ experiment. The constant $[CO_3^{2-}]$ data can be corrected using the independently measured empirical DIC correlation shown in Fig. 3a. Removing the influence of DIC from these data results in a $\delta^{11}B$-pH relationship for the constant $[CO_3^{2-}]$ experiment that is statistically indistinguishable from the constant pH experiment (Fig 4a). Thus, we show that skeletal $\delta^{11}B$ in our experiments are not solely a function of seawater pH, DIC, or $[CO_3^{2-}]$ (Fig. 3c), instead they can be parsed into separate additive pH and DIC effects. Regressions

365 against other carbonate system parameters also fail to identify a single master
366 parameter that can explain $\delta^{11}B$ on their own (Supplementary Fig. 4). Unlike $\delta^{11}B$,
367 skeletal B/Ca in cultured *B. elegans* follows a simple, precise ($R^2 = 0.95$), and
368 promising relationship with seawater DIC (Fig. 4b).

369 Our experiments show that a $\delta^{11}B$ DIC effect exists and that it can be
370 corrected. Indeed, our $\delta^{11}B$ paleo-pH calibration in *B. elegans*, which is valid for both
371 constant DIC and DIC corrected data, is promising because it is precise ($R^2= 0.93$)
372 compared to previous cold-water coral calibrations (Trotter, et al., 2011;
373 Anagnostou et al., 2012; McCulloch et al., 2012b; Stewart et al., 2016; Rae et
374 al.,2018), with an implied uncertainty for reconstructed pH of ± 0.05 pH units (1σ
375 prediction interval; Fig. 4b). The slope of this relationship matches other cold-water
376 coral calibrations (Supplemental Fig. 8). This similarity suggest that our high
377 precision slope and our mechanistic explanation for how corals record this signal –
378 discussed below - may be generalizable to other species. Furthermore, the
379 discovery of a DIC effect in *B. elegans* raises the question of whether other widely
380 used archives like foraminifera also show a separate DIC effect.
381
382
383 *3.2 Transmembrane boric acid diffusion*
384 The DIC effect has important implications for understanding how corals incorporate
385 boron and how to interpret $\delta^{11}B$ signals. We use our results to evaluate whether
386 $\delta^{11}B$ is primarily controlled by pH_{CF}. To this end, we first compare our $\delta^{11}B$ data to
387 studies in tropical corals where pH_{CF} was measured directly with pH-sensitive dyes.

When the tropical coral *S. pistillata* is cultured at constant pH, pH_{CF} increases with seawater DIC (Comeau et al., 2016). If skeletal $\delta^{11}B$ is primarily controlled by pH_{CF}, then $\delta^{11}B$ should also increase with DIC. We instead observe the opposite trend in $\delta^{11}B$ for cold-water corals (Fig. 3a). This contradictory observation suggests that $\delta^{11}B$ is influenced by factors other than just pH_{CF}, or that the relationship between seawater chemistry and pH_{CF} differs substantially between tropical symbiont-bearing (zooxanthellate) corals and cold-water non-symbiont-bearing corals. Either scenario requires a mechanism that can explain why skeletal $\delta^{11}B$ decreases with seawater DIC at constant seawater pH.

We invoke a new flux for boron during biomineralization, show that this flux can explain the counterintuitive DIC effect, and demonstrate that it can explain the sensitivity of skeletal $\delta^{11}B$ and B/Ca to external seawater parameters. A major species of dissolved boron in seawater is boric acid, $B(OH)_3$. Because boric acid is uncharged and relatively small, we propose that this species can diffuse through cell membranes in corals with a characteristic diffusion coefficient D_B. While boric acid diffusion is overlooked in many biomineralization models, it is recognized as an important flux in other organisms (Dordas and Brown, 2000). Including this diffusional flux has major implications for the interpretation of $\delta^{11}B$ in marine calcifiers.

Consider a hypothetical end member scenario where the timescale for boric acid diffusion through membranes is fast compared to other processes. Rapid diffusion between seawater and the calcifying fluid will lead to chemical and isotopic equilibration between boric acid in both pools. Thus boric acid in the

calcifying fluid will have the same $\delta^{11}B$ as boric acid in seawater. Because equilibrium isotope fractionation is established rapidly between boric acid and borate (Zeebe and Wolf-Gladrow, 2001), borate in the calcifying fluid will also have the same $\delta^{11}B$ as borate in seawater. This thought experiment shows how rapid diffusion translates a seawater pH signal to the borate ion in the calcifying fluid. This seawater pH signal would be maintained regardless of pH_{CF} and would be recorded in skeletal carbonates despite physiological control of calcification. The opposite end member scenario occurs if boric acid diffusion is slow enough to be insignificant, with boron sourced from flushing of the calcifying fluid by seawater exchange (Tambutte et al., 2012; Gagnon et al., 2012), or by any other transport process where isotopic fractionation is negligible. In this case, skeletal $\delta^{11}B$ will primarily be set by pH_{CF} and would be under direct physiological control. The former scenario with rapid diffusion, where skeletal $\delta^{11}B$ is primarily controlled by external pH, may explain why most foraminifera have shell $\delta^{11}B$ close to that of the borate ion at seawater pH, despite internal pH elevation in the calcifying fluid (Rae, 2018). By contrast, a situation where the balance between diffusion and seawater transport leads to offsets between skeletal $\delta^{11}B$ and seawater borate is more applicable to corals, as we will now show.

The two end member scenarios discussed above set bounds on skeletal $\delta^{11}B$ (Fig. 5a). The lower bound in Fig. 5a is a function of seawater pH; the upper bound is a function of pH_{CF}. Between these bounds, the balance between transmembrane diffusion and seawater exchange modulates skeletal $\delta^{11}B$. This balance is captured in the dynamical parameter D_B/kz, where k is the rate of seawater exchange such

that k^{-1} is the residence time of seawater in the calcifying fluid; and z is the volume to surface area ratio of the calcifying fluid, which is also the idealized thickness of the calcifying space if it were shaped like a box. These terms do not have to be known individually to predict $\delta^{11}B$ as it is changes in their non-dimensional ratio D_B/kz that can result in dramatic shifts in skeletal $\delta^{11}B$, even when both pH_{CF} and seawater pH are constant.

3.3 A general geochemical model for biomineralization

We hypothesize that the DIC effect in cold-water corals can be explained through an increase in the relative importance of diffusion (i.e. increase in D_B/kz) as seawater DIC increases rather than changes in pH_{CF}. This could occur for example, if seawater exchange with the calcifying fluid decreases with seawater DIC. To test if this postulated relationship can explain our data, and to explore why it might occur, we incorporated boron into a geochemical model of biomineralization. Once seawater conditions are specified, the resulting set of governing equations indicates that just three parameters are necessary to completely describe the boron and carbonate chemistry of the calcifying fluid: e.g. $D_B/$kz, pH_{CF}, and $P/kz\rho$. Here, the parameter $P/kz\rho$ represents the balance between skeletal calcification and seawater exchange, where P is the area normalized precipitation rate of mineral skeleton and ρ is the density of seawater. By varying these three parameters, we can systematically explore all possible combinations of the processes included within the model.

Using only the subset of data from our constant pH experiment, the three parameters are optimized so that modeled $\delta^{11}B$ and modeled mean B/Ca match

457 experimental results. In practice, our experimental $\delta^{11}B$ data inform the choice of
458 pH_{CF} and the mean D/kz; the $\delta^{11}B$-DIC effect determines the sensitivity of the D/kz
459 dependence on DIC; and $P/kz\rho$ is primarily controlled by the mean value of B/Ca.
460 Several combinations of parameters can explain our constant pH data. However,
461 once physically impossible fluxes are excluded and only actively calcifying states are
462 considered, the parameters cluster in a small region of model space.

463 We find that a simple set of model parameters can accurately predict the
464 trends and values across our dataset, illuminating two physiologically relevant rules
465 that can explain biomineralization in these corals. *Rule 1*: pH_{CF} is constant regardless
466 of external seawater chemistry. This rule is necessary to fit the entirety of our
467 dataset. A best-fit value is 8.95, but valid results are possible if $8.90 < pH_{CF} < 9.15$.
468 Within the model, cold-water corals maintain this target pH through alkalinity
469 pumping. The physiological significance of this pH is that it approaches pK_{a2} of the
470 carbonate system (9.3). When $pH = pK_{a2}$, buffer strength is maximized and
471 carbonate ion, the primary species that determines precipitation rate, becomes the
472 dominant species of DIC. *Rule 2*: The parameter D_B/kz increases linearly with DIC_{SW}.
473 This increase in D_B/kz implies a systematic decrease in seawater flushing at higher
474 DIC_{SW} if we consider that the boric acid diffusion coefficient is a biophysical
475 property of a membrane and is likely fairly constant (possible exceptions discussed
476 in Supplementary Materials). If a value for D_B is chosen so that modeled B/Ca
477 matches the average B/Ca taken across the corals cultured at constant pH, then this
478 D_B parameter also sets $P/kz\rho$. Our model applies this same constant value of D_B to all
479 corals.

Despite being trained only on the constant pH experiment, these two calcification rules accurately predict the $\delta^{11}B$ and B/Ca of the other two independent experiments without further fitting (Fig. 5b-d). Notably, the sensitivity of $\delta^{11}B$ to external pH and the dependence of B/Ca on seawater DIC, which are the basis of boron-paleoproxies, emerge from the model without tuning, without additional parameters, and even though the training set did not include any pH sensitivity. Thus, the $\delta^{11}B$ paleo-pH proxy and the B/Ca-DIC relationship are emergent properties that result from boric acid diffusion, even though biomineralization occurs at a pH different from seawater. The match between modeled and experimental results, even for very different conditions, highlights the ability of our model to capture the geochemistry of biomineralization in cold-water corals.

3.4 Skeletal $\delta^{11}B$ does not necessarily reflect changes in calcifying fluid pH

We show that it is possible to reproduce the $\delta^{11}B$ values in our study, which span 4.5 ‰, while maintaining a constant pH_{CF}. Thus $\delta^{11}B$ cannot be interpreted unequivocally to indicate pH_{CF}. While changes in skeletal $\delta^{11}B$ in some other corals may reflect changes in pH_{CF}, our work shows this is not a unique interpretation.

This way of thinking about coral $\delta^{11}B$ may also resolve a longstanding problem in coral geochemistry. Centers of calcification (COC) are structures within coral skeletons that represent new mineral nucleation events. They are an essential part of the calcification process because they act as the framework for new growth (Gladfelter, 2007). During COC formation, several geochemical indicators imply

elevated pH_{CF} and that the calcifying fluid is more closed with respect to seawater exchange (Robinson et al., 2014). If $\delta^{11}B$ were determined by pH_{CF}, then elevated pH should lead to higher $\delta^{11}B$ values. Instead, skeletal $\delta^{11}B$ is anomalously low in the COCs (Blamart et al., 2007). Our newly described boric acid diffusion mechanisms can resolve this apparent contradiction. Lower *kz* values, which are consistent with closed system behavior, will tend to increase *D/kz*, and decrease $\delta^{11}B$, matching observations. Thus, COCs may have anomalously low $\delta^{11}B$ because of changes in seawater flushing rather than pH_{CF}.

3.5 Responses of coral calcification to ocean acidification

Armed with an accurate geochemical model, we can predict the response of *B. elegans* to ocean acidification. To do this, we add an aragonite mineral growth law to the model as a function of the calcifying fluid saturation state (Ω_{CF}), with rate constants fit to previous inorganic experiments. Our model predicts that precipitation rate is primarily a function of DIC_{SW}. The reason for this calcification rate effect is that large changes in external DIC are translated into the calcifying fluid through seawater exchange. At constant pH_{CF}, DIC_{CF} sets $[CO_3^{2-}]$ and therefore DIC_{CF} also controls precipitation rate.

In the coral growth data from our study, which was not used to train the model, skeletal mass indeed increases with DIC and compares favorably with model predictions (Fig. 1). The calcification rate effect in our data set is so clear because we span a large range of DIC (3000 μmol kg^{-1}). Over smaller ranges of DIC, like those explored in typical OA experiments, the model predicts only small changes in

526 calcification rate. For example, in a prior culture experiment where *B. elegans* was
527 subjected to OA under controlled conditions, coral growth was resilient and showed
528 no significant change (Crook et al., 2013). Thus, without any additional tuning, the
529 model explains both the sensitivity and resilience of cold-water coral to a range of
530 environmental perturbations.

531 Our model shows that there is a hidden energetic cost for the apparent
532 resilience of calcification rate to OA in *B. elegans*. One model output is the ratio of
533 ion pumping (F) to calcification rate (P), which is a measure of efficiency. Higher F/P
534 values indicate that corals must expend more energy actively pumping ions per unit
535 of skeletal growth. The model shows that F/P increases under simulated OA,
536 modeled here as CO_2 uptake into seawater at constant alkalinity, which also lowers
537 the aragonite saturation state (Ω_{SW}). Our model thus predicts that corals require
538 more energy to calcify as a result of ocean acidification. Energy availability is known
539 to affect the response of coral to OA (for example, Edmunds 2011; Cohen and
540 Holcomb, 2015), and may explain an apparent sensitivity to OA in *B. europaea* near
541 low pH vents (Fantazzini et al., 2015). We provide a mechanism that predicts how
542 this energy requirement changes with environmental conditions and the relative
543 magnitude of this effect.

544 Precipitation rate itself is only weakly sensitive to OA in our model, therefore
545 the explanation for decreasing calcification efficiency must be systematic changes in
546 the amount of active ion pumping. The pumping flux is set by the vertical difference
547 between seawater alkalinity and calcifying fluid alkalinity in Fig. 6. When calcifying
548 fluid pH is constant, the pumping flux increases with ocean acidification and at

549 lower seawater aragonite saturation states. By contrast, precipitation rate is not as
550 sensitive to OA because lines of constant pH have a similar slope as lines of constant
551 [CO_3^{2-}]. Corals that follow a constant pH_{CF} strategy (*Rule 1*) will maintain similar
552 precipitation rates in the face of ocean acidification but feel this cost at the
553 organismal level in the form of increased energy needs to accommodate extra
554 pumping.

555 The emergent property that coral calcification is indirectly sensitive to Ω_{SW} is
556 consistent with experimental observations, as skeletal growth in both tropical coral
557 (Schneider and Erez, 2006) and other calcifying organisms (Waldbusser et al., 2015)
558 responds primarily to Ω_{SW}. To the extent that our model applies to these other
559 calcifiers, our approach indicates that the Ω_{SW} effect is driven by energetic demands
560 at the organismal scale rather than a direct impact on precipitation rate. However,
561 there are differences between cold-water and symbiont-bearing tropical corals,
562 which may hint at other ion pumping strategies. For example, we know that tropical
563 corals do not always maintain a constant pH_{CF} (Venn et al., 2013; Comeau et al.,
564 2016). Speculatively, these tropical corals could maintain a constant amount of ion
565 pumping rather than the target pH_{CF} (Cohen et al., 2009). This constant pumping
566 strategy would help limit the runaway energetic costs of OA, but would also make
567 instantaneous precipitation rates much more sensitive to OA. Our modeling
568 framework shows how different calcification strategies incur specific costs during
569 OA, which could lead to divergent impacts and require different pathways to
570 resilience. Within this framework, each strategy also implies testable relationships
571 between seawater chemistry, growth rates, skeletal elemental composition (Gagnon

et al., 2013), pH_{CF}, and $\delta^{11}B$. Indeed, a constant pumping rule can qualitatively explain trends in existing pH-dye datasets for tropical corals, including divergent responses to constant pH (Comeau et al., 2016) and constant ALK (Venn et al., 2013) experiments. However, a more quantitative evaluation of this hypothesis awaits culture experiments where both boron geochemistry and pH_{CF} are measured in tropical coral. Through a detailed picture of the connection between environmental conditions and calcification physiology, our approach can explain skeletal geochemistry, $\delta^{11}B$-pH proxy sensitivity, and the response of calcification to an acidifying ocean.

582 **References**
583
584 Al-Horani, F., Al-Moghrabi, S. & de Beer D. The mechanism of calcification and its
585 relation to photosynthesis and respiration in the scleractinian coral *Galaxea*
586 *fascicularis*. *Mar. Biol.* **142**, 419–426 (2003).
587
588 Allemand D., et al. Biomineralisation in reef-building corals: from molecular
589 mechanisms to environmental control. *C. R. Palevol.* **3**, 453-467 (2004).
590
591 Anagnostou, E., et al. Evaluation of boron isotope ratios as a pH proxy in the deep
592 sea coral *Desmophyllum dianthus*: evidence of physiological pH adjustment. *Earth*
593 *Planet. Sci. Lett*. **349-350**, 251-260 (2012).
594
595 Blamart, D., et al. Correlation of boron isotopic composition with ultrastructure in
596 the deep-sea coral Lophelia pertusa: Implications for biomineralization and paleo-
597 pH. *Geochem. Geophys. Geosys.* **8**, Q12001 (2007).
598
599 Branson, O. Boron Incorporation into Marine CaCO3 Boron Incorporation into
600 Marine CaCO3. In: Marschall H., Foster G. (eds) Boron Isotopes. Advances in Isotope
601 Geochemistry. Springer (2018).
602
603 Cai et al., Microelectrode characterization of coral daytime interior pH and
604 carbonate chemistry. *Nature Communications* **7**, 11144 (2016).
605
606 Chen, S., Gagnon, A., Adkins, J. Carbonic anhydrase, coral calcification and a new
607 model of stable isotope vital effects. *Geochim. Cosmochim. Acta* **236**, 179-197
608 (2018).
609
610 Cohen et al., Morphological and compositional changes in the skeletons of new coral
611 recruits reared in acidified seawater: Insights into the biomineralization response to
612 ocean acidification. *Geochem. Geophys. Geosys*. **10**, Q07005 (2009).
613
614 Cohen, A. and Holcomb, M. Why corals care about ocean acidification: Uncovering
615 the mechanism. *Oceanography* 22(4):118–127 (2015).
616
617 Comeau, S, et al. Coral calcifying fluid pH is modulated by seawater carbonate
618 chemistry not solely seawater pH. *Proc. R. Soc. B* **284**, 20161669 (2016).
619
620 Comeau, S. et al. Resistance to ocean acidification in coral reef taxa is not gained by
621 acclimatization. *Nature Climate Change* **9**, 477-483 (2019).
622
623 Crook, E., et al. Impacts of food availability and pCO2 on planulation, juvenile
624 survival, and calcification of the azooxanthellate scleractinian coral *Balanophyllia*
625 *elegans*. Biogeosciences 10, 7599-7608 (2013).
626

Dordas, C. & Brown, P.H., Permeability of boric acid across lipid bilayers and factors affecting it. *The Journal of membrane biology* **175**, 95-105 (2000).

Durham, J. W., and Barnard, J. Stony corals of the Eastern Pacific collected by the Velero III and Velero IV. *Allan Hancock Pacific Expeditions* **16**, 1-110 (1952).

Edmunds P. Zooplanktivory ameliorates the effects of ocean acidification on the reef coral *Porites* spp. *Limnol. Oceanogr.* **56**, 2402-2410 (2011).

Fantazzini et al. Gains and losses of coral skeletal porosity changes with ocean acidification acclimation. *Nature Comm.* **6**:7785 (2015).

Farmer, J. et al. Boric acid and borate incorporation in inorganic calcite inferred from B/Ca, boron isotopes and surface kinetic modeling. *Geochim. Cosmochim. Acta* **244**, 229-247 (2019).

Foster, G. Seawater pH, pCO2 and [CO_3^{2-}] variations in the Caribbean Sea over the last 130 kyr: a boron isotope and B/Ca study of planktonic foraminifera. *Earth Planet. Sci. Lett.* **271**, 254-266 (2008).

Gagnon, A., Adkins, J, & Erez, J. Seawater transport during coral biomineralization. *Earth Planet. Sci. Lett.* **329-330**, 150-161 (2012).

Gagnon, A., et al. Sr/Ca sensitivity to aragonite saturation state in culturedsubsamples from a single colony of coral: Mechanismof biomineralization during ocean acidification. *Geochim. Cosmochim. Acta* **105**, 240–254 (2013).

Gerrodette T. Equatorial Submergence in a Solitary Coral, *Balanophyllia elegans*, and the Critical Life Stage Excluding the Species from Shallow Water in the South. *Mar. Ecol. Prog. Ser.* 1, 227–235 (1979).

Giri, S., Swart, P., Pourmand, A. The influence of seawater calcium ions on coral calcification mechanisms: Constraints from boron and carbon isotopes and B/Ca ratios in *Pocillopora damicornis*. *Earth Planet. Sci. Lett.* **519**, 130–140 (2019).

Gladfelter, B. Skeletal development in *Acropora palmata* (Lamarck 1816): a scanning electron microscope (SEM) comparison demonstrating similar mechanisms of skeletal extension in axial versus encrusting growth. *Coral Reefs* **26**, 883-892 (2007).

Gothmann, A., et al. Fossil corals as an archive of secular variations in seawater chemistry since the Mesozoic . *Geochim. Cosmochim. Acta* **160**, 188-208 (2015).

Hemming, N., and Hanson, G. Boron isotopic composition and concentration in modern marine carbonates. *Geochim. Cosmochim. Acta* **56**, 537–543 (1992).

673 Hemming, N., Hönisch, B. Boron isotopes in marine carbonate sediments and the pH
674 of the ocean. In: Hillaire–Marcel, C., de Vernal, A. (Eds.), Developments in Marine
675 Geology. Elsevier, pp. 717–734 (2007).
676
677 Holcomb et al., Factors affecting B/Ca ratios in synthetic aragonite. *Chem. Geol.* **437**,
678 67-76 (2016).
679 Kiss, E. Ion-exchange separation and spectrophotometric determination of boron in
680 geological materials. *Anal. Chim. Acta* **211**, 243-256 (1988).
681
682 Klochko et al. Experimental measurement of boron isotope fractionation in
683 seawater. *Earth Planet. Sci. Lett.* **248**, 276-285 (2006).
684
685 McConnaughey T. ^{13}C and ^{18}O isotopic disequilibrium in biological carbonates. 2. In
686 vitro simulation of kinetic isotope effects. *Geochim. Cosmochim. Acta* **53**, 151–162
687 (1989).
688
689 McCulloch, M., Falter, J., Trotter, J., Montagna, P. Coral resilience to ocean
690 acidification and global warming through pH up-regulation. *Nature Climate Change*
691 **2**, 623-627 (2012a).
692
693 McCulloch, M., et al. Resilience of cold-water scleractinian corals to ocean
694 acidification: Boron isotopic systematics of pH and saturation state up-regulation.
695 *Geochim. Cosmochim. Acta* **87**, 21-34 (2012b).
696
697 McCulloch et al. Coral calcification in a changing World and the interactive dynamics
698 of pH and DIC upregulation. *Nature Communications* **8**, 15686
699 (2017).
700
701 Misra, S., et al. Determination of δ B by HR-ICP-MS from mass limited samples:
702 application to natural carbonates and water samples. *Geochim. Cosmochim. Acta*
703 **140**, 531–552 (2014).
704
705 Murray, J.W., et al. An inland sea high nitrate-low chlorophyll (HNLC) region with
706 naturally high pCO2. *Limnology and Oceanography* **60**, 957-966 (2015) .
707
708 Nicola, A., et al. The effect of ocean acidification on tropical coral calcification:
709 Insights from calcification fluid DIC chemistry. *Chem. Geol.* **497**, 162-169 (2018).
710
711 Noireaux, J., et al. Crystallographic control on the boron isotope paleo-pH proxy.
712 *Earth Planet. Sci. Lett.* **430**, 398–407 (2015).
713
714 Olsen et al., The Global Ocean Data Analysis Project version 2 (GLODAPv2) – an
715 internally consistent data product for the world ocean. *Earth Syst. Sci. Data* **8**, 297-
716 323 (2016).
717

718 Pandolfi, J.M., Connolly, S.R., Marshall, D.J., & Cohen, A.L. Projecting Coral Reef
719 Futures Under Global Warming and Ocean Acidification. *Science* **333**, 418-422
720 (2011).
721
722 Rae, J. et al., CO_2 storage and release in the deep Southern Ocean on millennial to
723 centennial timescales. *Nature* **562**, 569-573 (2018).
724
725 Rae, J. Boron Isotopes in Foraminifera: Systematics, Biomineralisation,
726 and CO2 Reconstruction. In: Marschall H., Foster G. (eds) Boron Isotopes. Advances
727 in Isotope Geochemistry. Springer (2018).
728
729 Robinson, L., et al. The geochemistry of deep-sea coral skeletons: A review of vital
730 effects and applications for palaeoceanography. *Deep-Sea Research* II **99**, 184-198
731 (2014).
732
733 Rodolfo-Metalpa, R. et al., Calcification is not the Achilles' heel of cold-water corals
734 in an acidifying ocean. *Global Change Biology* **21**, 2238-2248 (2015).
735
736 Schneider, K., & Erez, J. The effect of carbonate chemistry on calcification and
737 photosynthesis in the hermatypic coral *Acropora eurystoma*. *Limonol. Oceanogr*. 51,
738 1284-1293 (2006).
739
740 Stewart, J, Anagnostou, E., and Foster, G. An improved boron isotope pH proxy
741 calibration for the deep-sea coral *Desmophyllum dianthus* through sub-sampling of
742 fibrous aragonite. Chem. Geol. **447**, 148-160 (2016).
743
744 Tambutte, E., et al. Calcein labelling and electrophysiology: insights on coral tissue
745 permeability and calcification. *Proc. R. Soc. B.* **279**, 19-27 (2012).
746
747 Trotter, J. et al. Quantifying the pH 'vital effect' in the temperate zooxanthellate coral
748 Cladocora caespitosa: Validation of the boron seawater pH proxy. *Earth Planet. Sci.*
749 *Lett.* **303**, 163–173 (2011).
750
751 Venn et al., Impact of seawater acidification on pH at the tissue–skeleton interface
752 and calcification in reef corals. *Proceedings of the National Academy of Sciences* **110**,
753 1634-1639 (2013).
754
755 Waldbusser, G., et al. Saturation-state sensitivity of marine bivalve larvae to ocean
756 acidification. *Nature Climate Change* **5**, 273-280 (2015).
757
758 Zeebe, R., Wolf-Gladrow, D. CO_2 in Seawater: Equilibrium, Kinetics, Isotopes. In:
759 Halpern, D. (Ed.), *Elsevier Oceanography Series* **65** (2001).
760
761 Zoccola, D., Tambutte, E. & Kulhanek, E. Molecular cloning and localization of a
762 PMCA P-type calcium ATPase from the coral *Stylophora pistillata*. *Biochim. Biophys.*
763 *Acta* **1663**, 117–126 (2004).

Acknowledgements

This research was supported in part by a National Science Foundation CAREER Award (1552694) and a University of Washington Royalty Research Fund Award, both to A.C.G. A postdoctoral fellowship to A.M.G from the Joint Institute for the Study of the Atmosphere and Ocean also supported this research. We thank C. Coath and R.C.J. Steele for analytical support.

Author Contributions

A.C.G and A.M.G conceived the study. A.M.G conducted the cold-water coral culture experiments. A.C.G, A.M.G, and O.B developed the geochemical model. J.A.S and J.W.B.R. analyzed coral skeletons for boron concentration and boron isotopes. A.C.G. wrote the original manuscript and programed the numerical model. All authors contributed to discussions about data interpretation, manuscript revisions, and data analysis.

780 **Figures and Captions**
781

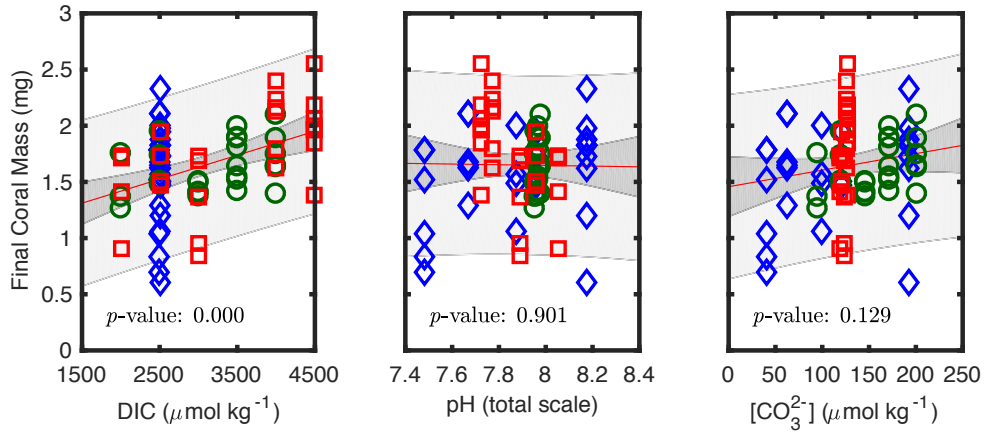

782
783

784 **Fig. 1.** Relationships between the final skeletal mass of each coral and culture water
785 chemistry. Symbols correspond to independent culture experiments and follow the
786 same scheme as the main paper: constant pH (green circles), constant DIC (blue
787 diamonds), or constant [CO_3^{2-}] (red squares). In total, 80 individuals were weighed.
788 All of the coral masses were fit against the respective culture parameters using an
789 un-weighted least square linear regression (red line). The 95 % level of confidence
790 (LOC) prediction interval (light gray region) and the 95 % LOC for the model
791 parameters (dark gray region) are also shown. Only the relationship between
792 skeletal mass and DIC is significant at the >95 % LOC (leftmost panel).
793

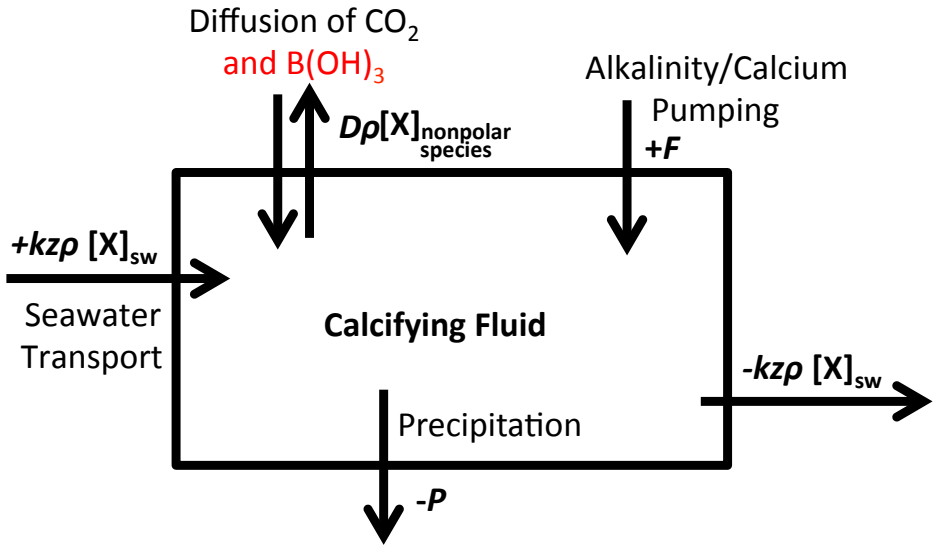

794
795 **Fig. 2.** Box model of coral biomineralization with key fluxes.
796

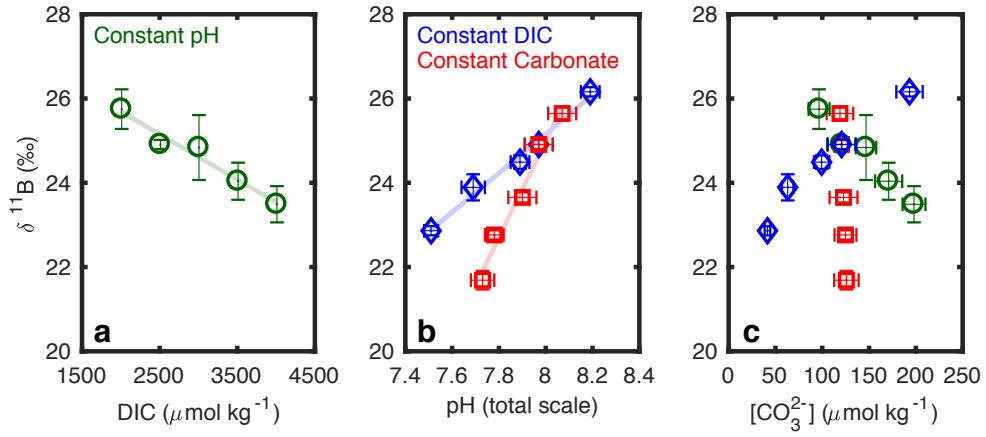

Fig. 3. Skeletal $\delta^{11}B$ across a range of seawater carbonate chemistry conditions for the cultured cold-water coral *B. elegans*. **a,** When seawater pH is held constant, skeletal $\delta^{11}B$ is not constant and instead decreases systematically with seawater DIC: $\delta^{11}B = -1.08$ DIC (mmol/kg) + 27.85. **b,** $\delta^{11}B$ is more steeply sensitive to pH when $[CO_3^{2-}]$ is held constant (red squares) as compared to the separate experiment where DIC is held constant (blue diamonds). Lines indicate best fit to skeletal data. **c**, The apparent relationships between $\delta^{11}B$ and environmental parameters can yield conflicting results due to a combination of pH and DIC effects, as shown when $\delta^{11}B$ is plotted vs. $[CO_3^{2-}]$. Only those horizontal error bars that are larger than symbols are shown (2σ std. dev. of culture solution measurements). Data points represent average $\delta^{11}B$ of 1 to 3 different corals from the same culture conditions with propagated analytical and replicate error (1σ std. err.).

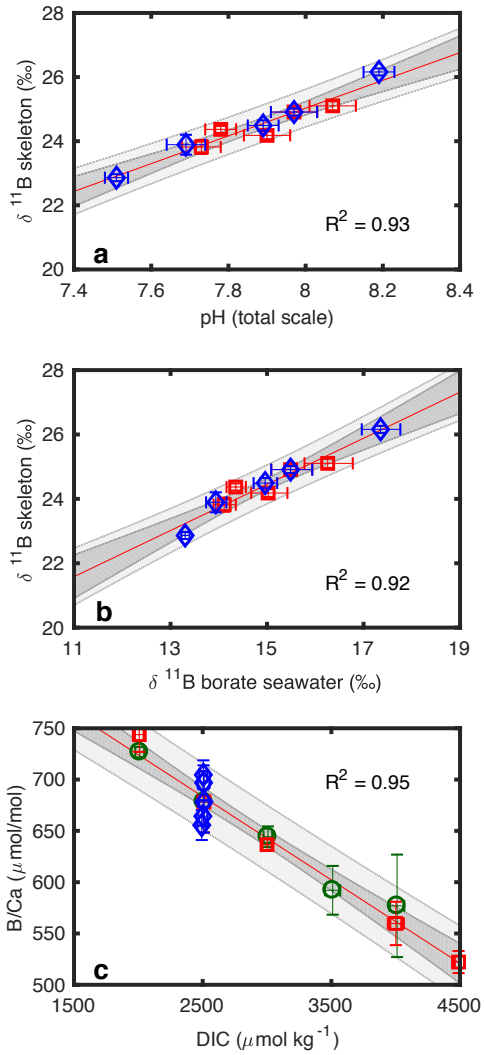

Fig 4. Calibrations of the $\delta^{11}B$-pH proxy and B/Ca-DIC proxy in the cultured cold-water coral *B. elegans*. **a**, Boron isotope paleo pH calibration ($\delta^{11}B = 4.33pH - 9.60$) including data from the constant DIC experiment (blue diamonds) and corrected data from the constant carbonate ion experiment (red squares; $\Delta(\delta^{11}B) = (DIC - 2.5$ mmol/kg)×1.08). The residual of the fit is indistinguishable from instrumental uncertainty. Both the prediction interval (light gray) and fit uncertainty (dark gray) are shown at the 95 % level of confidence. **b,** Calibration between skeletal $\delta^{11}B$ and seawater borate $\delta^{11}B$ ($\delta^{11}B_{skeletal} = 0.717 \times \delta^{11}B_{borate} + 13.70$). **c**, Skeletal Boron/Calcium follows seawater DIC: B/Ca = −81.3 DIC (mmol/kg) + 887.

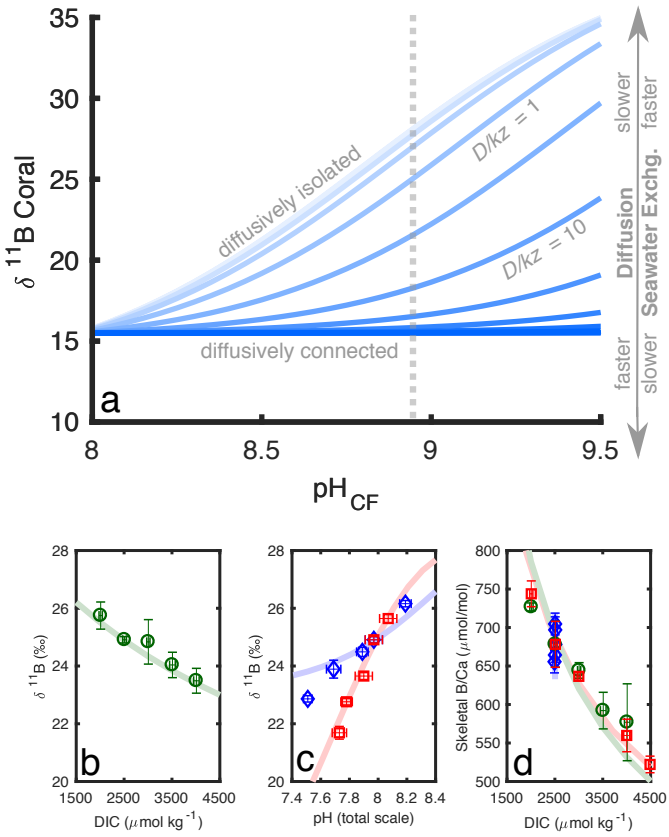

Fig. 5. Models that include boric acid diffusion can explain skeletal $\delta^{11}B$ even when calcifying fluid pH is constant. **a**, Analytical model of skeletal $\delta^{11}B$ at constant seawater pH (ambient seawater pH = 7.96). Each curve corresponds to a different value of D_B/kz. As diffusion rates increase relative to seawater transport, $\delta^{11}B$ decreases, even when pH_{CF} and seawater pH are constant (vertical dashed line at pH_{CF} = 8.95). Changes in seawater pH (not shown) will shift the dark blue lower bound vertically, which links seawater chemistry to skeletal $\delta^{11}B$. Because changes in this lower bound squeeze or expand the family of curves, skeletal $\delta^{11}B$ is sensitive to both seawater pH and D_B/kz, even when pH_{CF} is constant. **b**, Our numerical model (Supplementary Material Model Scenario B) uses a constant pH_{CF}=8.95 and was trained with only the $\delta^{11}B$ data of the constant pH experiment (green line, panel b) and the mean B/Ca value (mean of data points in panel d). **c**, Without additional fitting, the model skillfully predicts the $\delta^{11}B$-pH relationships in the separate constant DIC and constant carbonate ion experiments (blue and red lines, respectively, panel c). The prediction is very accurate for seawater pH values between 7.7 and 8.1. The extreme data points still follow the model closely when the model is blind to these data (shown here), and can be matched exactly with the same pH_{CF} if we tune model parameters to these results (not shown). **d**, The model also predicts the B/Ca-DIC slope without fitting to this relationship.

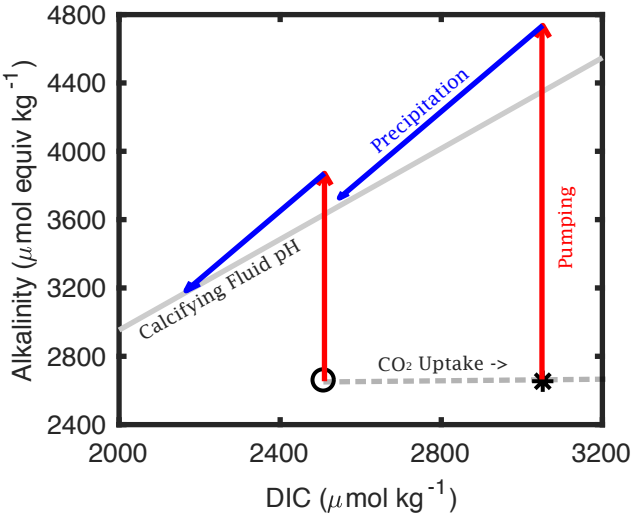

Fig. 6. Changes in seawater chemistry affect calcification efficiency. From a given starting seawater composition (circle or star), internal pH is elevated via alkalinity pumping (red vectors). Precipitation then occurs (blue vectors), drawing down alkalinity relative to dissolved inorganic carbon in a 2:1 ratio, until reaching a constant calcifying fluid pH (grey line). Under ocean acidification, carbon dioxide invasion shifts seawater chemistry along the horizontal gray dashed line from ambient conditions (black circle) to acidified conditions (black star). Calcifying fluid chemistry is constrained to pH_{CF} = 8.95 (solid line) if corals follow the rules in our model. Therefore, changes in the seawater starting point affect the amount of active alkalinity pumping required to reach this line, which is reflected in the different lengths of the vertical red vectors. By contrast, the length of the blue precipitation vectors change by a relatively smaller amount. More pumping for similar amounts of precipitation means lower calcification efficiency. For clarity the extent of ocean acidification is exaggerated in this example compared to near term projections, but the same efficiency effects apply to smaller levels of acidification.

868 **Table 1.** Coral culture conditions.
869

Condition (Experinment #)	DIC	2s SD	ALK	2s SD	pH	2s SD	$[CO_3^{2}]$	2s SD	$\delta^{11}B$ Borate Ion (Calculated)
	(µmol/kg)		(µmol/kg)		(total scale)		(µmol/kg)		‰
Common (1)	2510	38	2648	42	7.97	0.06	121	15	15.49
Constant DIC (2)	2492	35	2474	19	7.51	0.03	41	3	13.30
Constant DIC (3)	2501	35	2540	16	7.69	0.05	63	6	13.94
Constant DIC (4)	2507	46	2608	25	7.89	0.04	99	8	14.96
Constant DIC (5)	2505	32	2754	20	8.19	0.04	193	14	17.35
Constant pH (6)	2011	35	2129	23	7.97	0.06	97	11	15.49
Constant pH (7)	3007	34	3170	22	7.98	0.04	147	11	15.56
Constant pH (8)	3510	59	3688	24	7.98	0.04	171	14	15.56
Constant pH (9)	4011	57	4211	29	7.99	0.03	198	12	15.63
Constant $[CO_3^{2-}]$ (10)	2007	33	2166	16	8.07	0.06	119	14	16.26
Constant $[CO_3^{2-}]$ (11)	3000	35	3128	18	7.9	0.06	123	15	15.02
Constant $[CO_3^{2-}]$ (12)	4001	63	4087	27	7.78	0.04	125	12	14.35
Constant $[CO_3^{2-}]$ (13)	4488	29	4562	20	7.73	0.05	126	13	14.11

870
871

872
873 **Table 2.** Boron isotope and B/Ca of cultured coral skeletons.
874

Sample ID	Condition	Skeletal $\delta^{11}B$ ‰	B/Ca µmol/mol	Skeletal $\delta^{11}B$ with DIC Correction ‰
1B-III	Common (1)	24.95	669	
1C-I	Common (1)	24.87	687	
2A-II	Constant DIC (2)	22.78	660	
2B-II	Constant DIC (2)	22.94	651	
3C-I	Constant DIC (3)	23.58	652	
3C-III	Constant DIC (3)	24.20	677	
4B-I	Constant DIC (4)	24.49	697	
5B-II	Constant DIC (5)	26.21	702	
5C-II	Constant DIC (5)	26.11	707	
6A-I	Constant pH (6)	26.21	729	
6B-II	Constant pH (6)	25.28	724	
7A-III	Constant pH (7)	24.07	626	
7C-II	Constant pH (7)	25.61	663	
8C-III	Constant pH (8)	24.04	592	
9A-III	Constant pH (9)	23.92	616	
9B-III	Constant pH (9)	23.06	537	
10C-II	Constant $[CO_3^{2-}]$ (10)	25.64	744	25.10
11A-I	Constant $[CO_3^{2-}]$ (11)	23.53	631	24.06
11A-III	Constant $[CO_3^{2-}]$ (11)	23.77	642	24.30
12A-IIII	Constant $[CO_3^{2-}]$ (12)	22.84	551	24.44
12B-II	Constant $[CO_3^{2-}]$ (12)	22.69	569	24.29
13A-I	Constant $[CO_3^{2-}]$ (13)	21.50	507	23.62
13B-I	Constant $[CO_3^{2-}]$ (13)	22.12	522	24.25
13B-III	Constant $[CO_3^{2-}]$ (13)	21.44	538	23.57

875

Supplementary Material 1

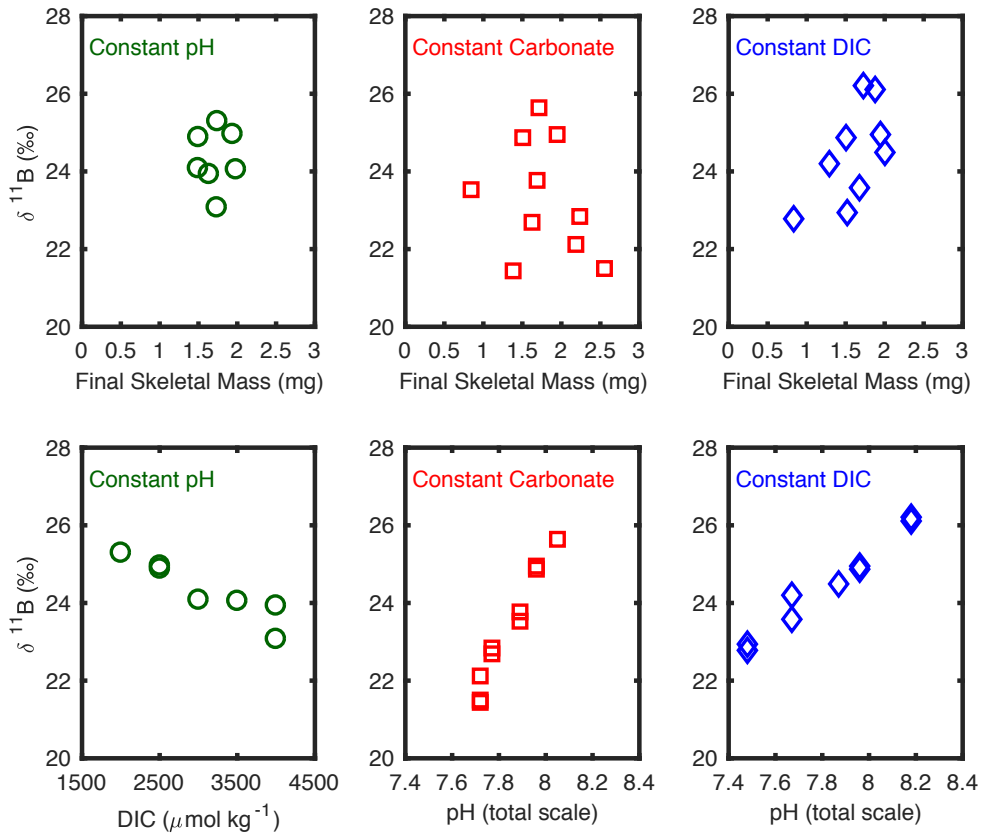

Supplemental Fig. 1 | Effect of sample mass on skeletal $\delta^{11}B$. Symbols correspond to independent culture experiments and follow the same scheme as the main paper: constant DIC (blue diamonds, top row), constant pH (green circles, second row), and constant $[CO_3^{2-}]$ (red squares, third row). These data show that the strong and systematic trends in $\delta^{11}B$ as a function of DIC and pH (bottom row) cannot be explained by a sample mass effect (top row). All individual coral data points are shown here. Duplicates from the same conditions are averaged in the figures for the main text.

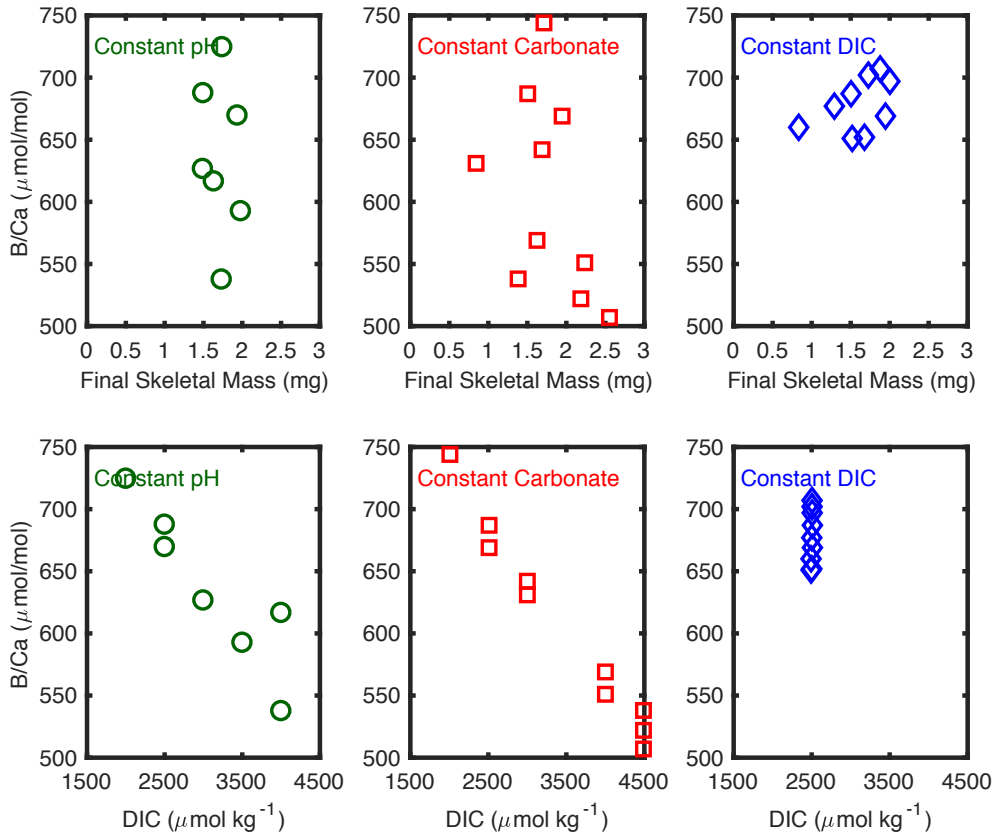

Supplemental Fig. 2 | Effect of sample mass on skeletal B/Ca. Symbols correspond to independent culture experiments and follow the same scheme as the main paper: constant DIC (blue diamonds, top row), constant pH (green circles, second row), and constant [CO_3^{2-}] (red squares, third row). These data show that the strong and systematic trends in B/Ca as a function of DIC (bottom row) cannot be explained by a sample mass effect (top row). The constant DIC experiment may show some evidence for a mixing relationship, but if present, this effect this does not change our conclusions other than providing another possible explanation for the anomalous scatter in the constant DIC experiment. All individual coral data points are shown here. Duplicates from the same conditions are averaged in the figures for the main text.

Empirical geochemical trends are summarized in Supplemental Figures 3-6. Note that the scientific method cannot unequivocally prove that pH and DIC or any other set of parameters ultimately control for $\delta^{11}B$. What these experimenst can prove is that neither seawater pH, seawater DIC, nor seawater $[CO_3^{2-}]$ control $\delta^{11}B$ by itself. Assigning the observed effect to pH and DIC rather than, for example, pH and $[CO_3^{2-}]$ has no effect on our conclusions since these effects are not explicitly identified in the model. Instead, the model uses the full carbonate chemistry of seawater, which is unique.

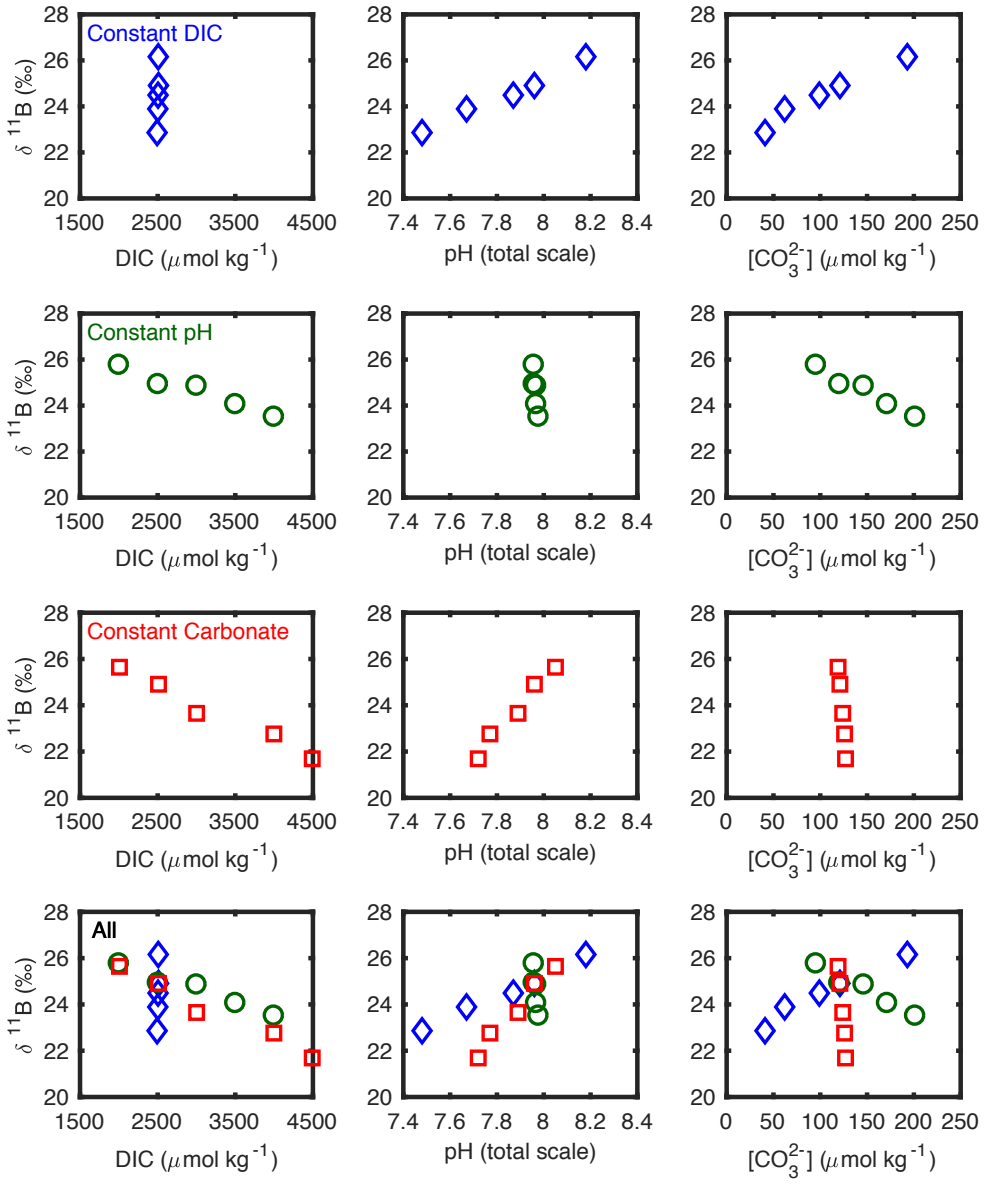

Supplemental Fig. 3 | Relationships between skeletal $\delta^{11}B$ and culture water chemistry. Symbols correspond to independent culture experiments and follow the same scheme as the main paper: constant DIC (blue diamonds, top row), constant pH (green circles, second row), and constant [CO_3^{2-}] (red squares, third row).

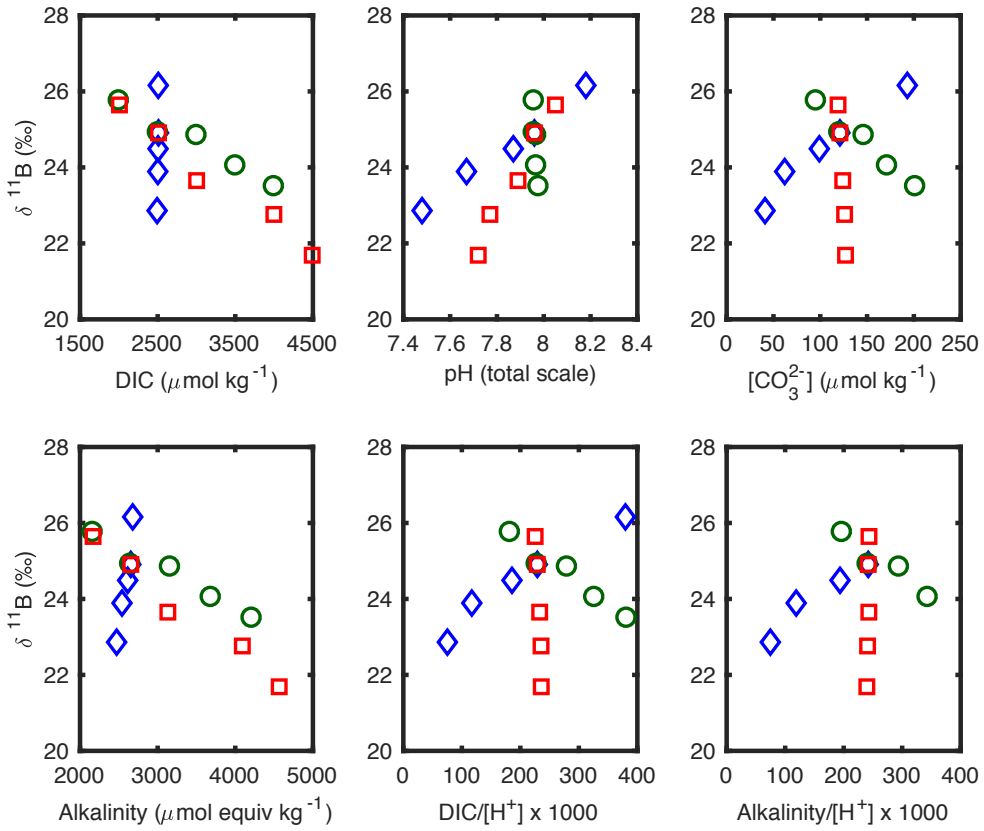

Supplemental Fig. 4 | Relationships between skeletal $\delta^{11}B$ and various culture water parameters. Symbols correspond to independent culture experiments and follow the same scheme as the main paper: constant DIC (blue diamonds, top row), constant pH (green circles, second row), and constant [CO_3^{2-}] (red squares, third row).

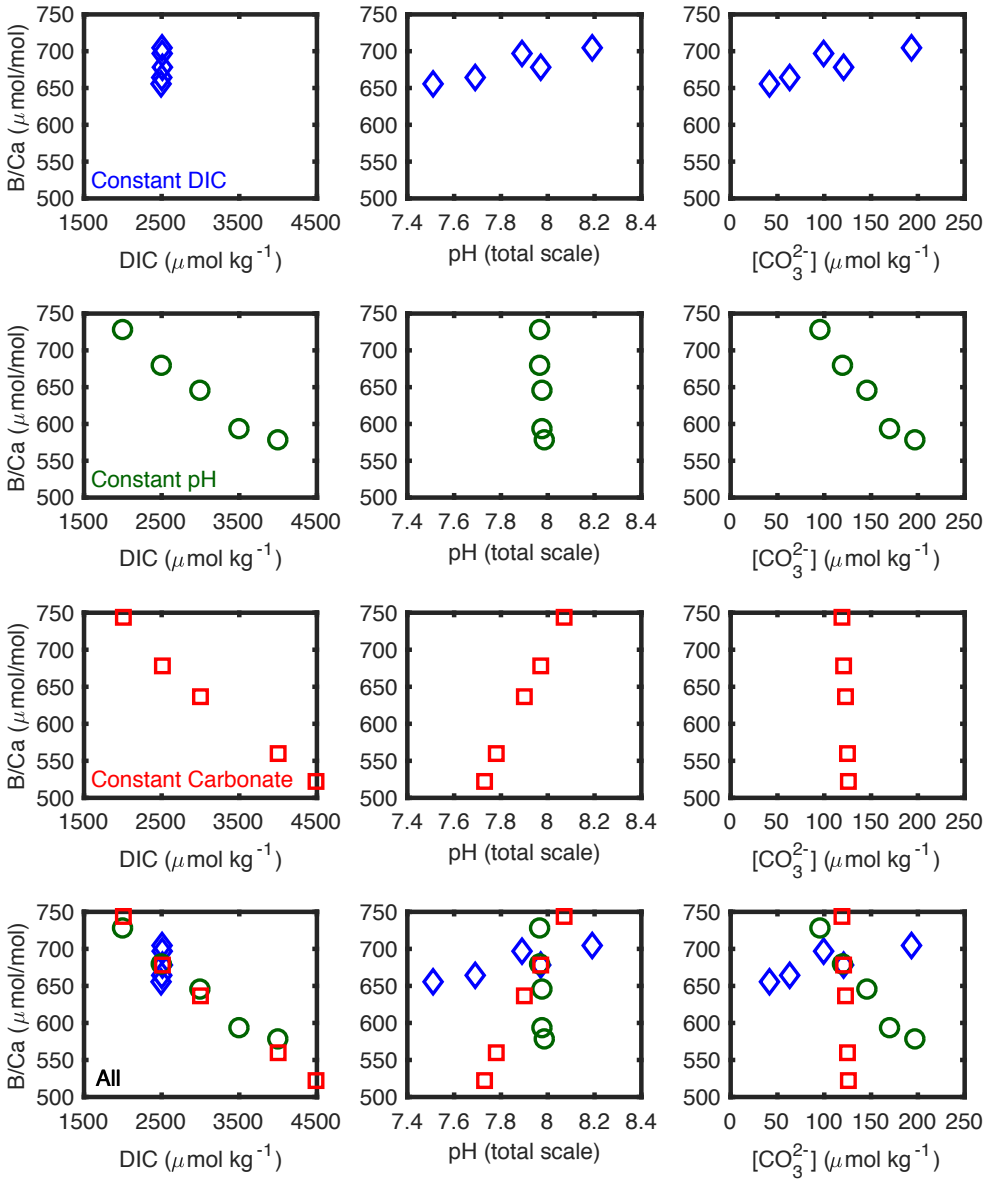

925
926 **Supplemental Fig. 5 | Relationships between skeletal B/Ca and culture water**
927 **chemistry.** Symbols correspond to independent culture experiments and follow the
928 same scheme as the main paper: constant DIC (blue diamonds, top row), constant
929 pH (green circles, second row), and constant [CO_3^{2-}] (red squares, third row).
930
931

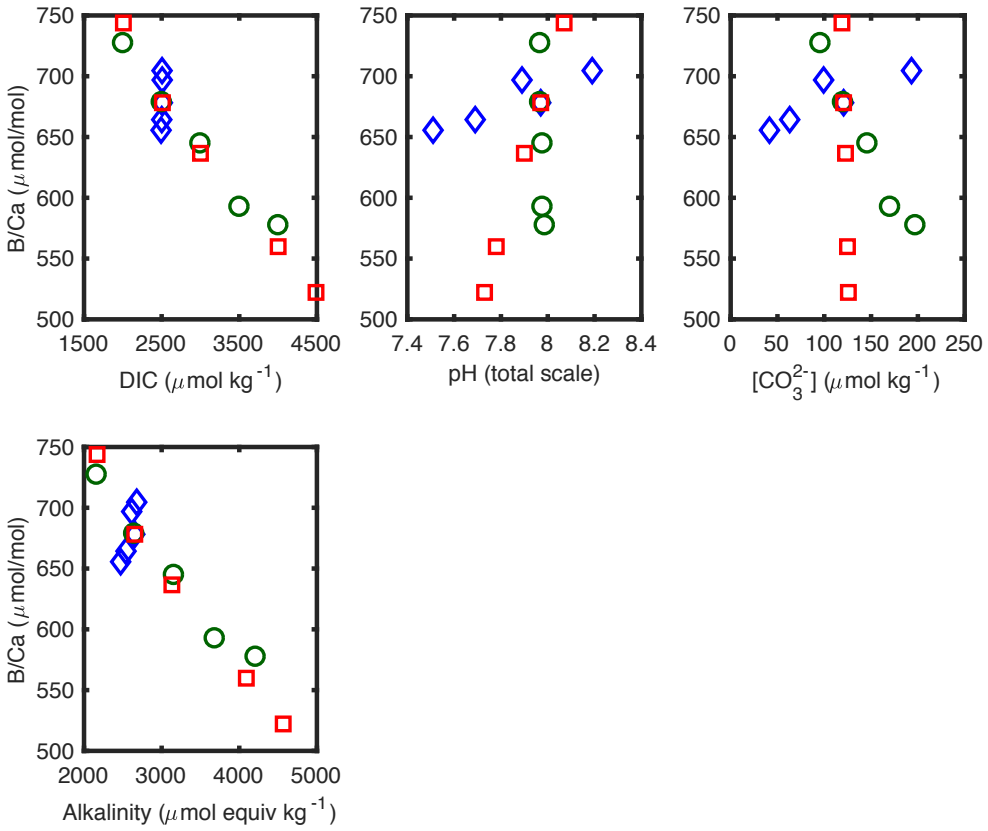

Supplemental Fig. 6 | Relationships between skeletal B/Ca and various culture water parameters. Symbols correspond to independent culture experiments and follow the same scheme as the main paper: constant DIC (blue diamonds, top row), constant pH (green circles, second row), and constant [CO_3^{2-}] (red squares, third row).

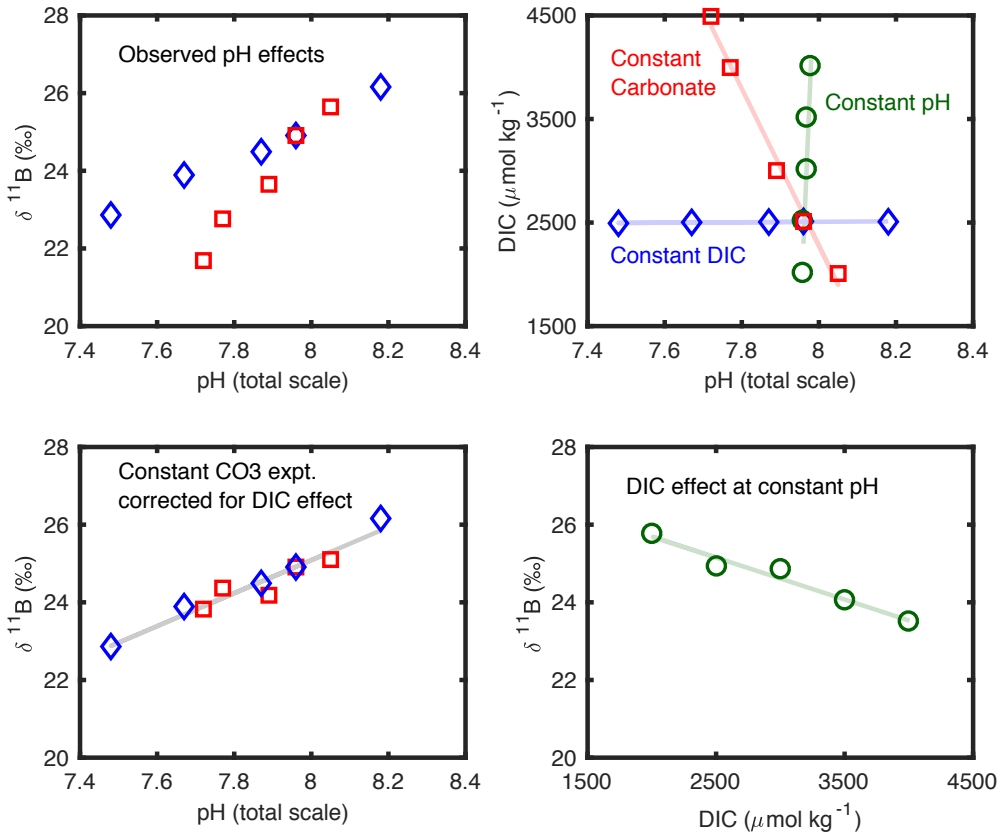

Supplemental Fig. 7 | Empirical correction for DIC effect. Upper left: Skeletal $\delta^{11}B$ has a steeper sensitivity to pH in the constant [CO_3^{2-}] experiment (red squares) when compared with the separate constant DIC experiment (blue diamonds). This would lead to different apparent paleo pH calibrations. **Upper right:** A key difference between these calibrations is that both pH and DIC change in the constant [CO_3^{2-}] experiment, but DIC does not change in the DIC experiment and pH does not change in the constant pH experiment. **Lower right:** An empirical DIC effect can be calibrated using the constant pH experiment, such that $\Delta(\delta^{11}B) = 1.08^* \Delta DIC$ (mmol/kg) at constant pH. **Lower left:** If this empirical correction is applied to the constant [CO_3^{2-}] experiment, then only the pH effect should be left. Indeed the [CO_3^{2-}] experiment with the DIC effect removed and the separate constant DIC experiment now show the same sensitivity to pH. Thus, $\delta^{11}B$ in cold-water coral can be parsed into separate pH and DIC effects. Our experiments show that $\delta^{11}B$ in cold-water coral is not solely a function of pH, DIC, or [CO_3^{2-}], but can be explained using two of these parameters.

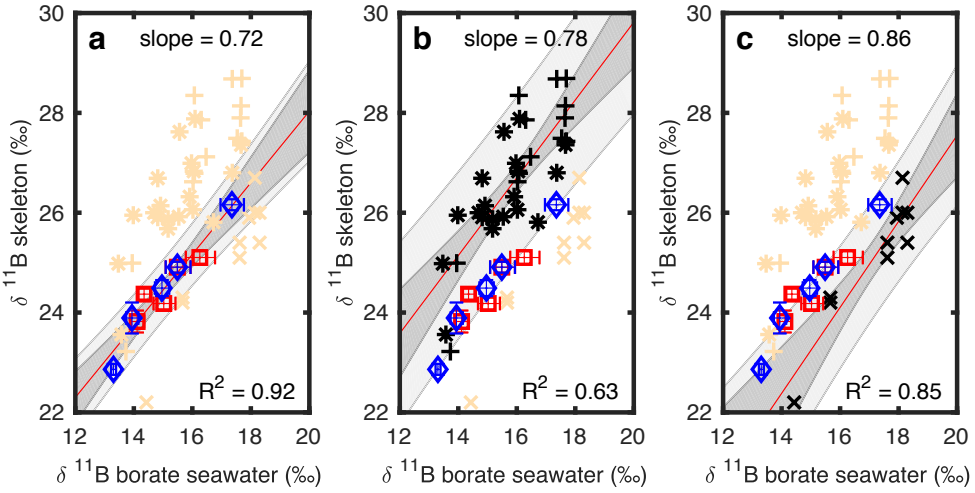

Supplemental Fig. 8 | Skeletal $\delta^{11}B$ is similarly sensitive to changes in seawater borate $\delta^{11}B$ for *B. elegans*, other symbiont-free cold water corals, and a temperate symbiont-bearing coral (*Cladocora caespitosa*). Skeletal $\delta^{11}B$ is plotted as a function of seawater borate $\delta^{11}B$ so that measurement across a range of depths, temperatures, and salinities can be compared. **a,** Linear fit with confidence interval and prediction interval for the constant DIC (blue diamonds) and the DIC-corrected constant carbonate ion experiment (red squares) from cultured *B. elegans* (data from this study; Fig. 3 of the main text: $\delta^{11}B_{skeletal} = 0.717 \times \delta^{11}B_{borate} + 13.70$). Also shown in gold symbols are previously reported stony coral data. Asterisks are measurements of wild collected *Desmophyllum dianthus*, a symbiont-free (azooxanthellate) deep-sea stony coral that is commonly used in paleoceanography (Rae et al., 2018; McCulloch et al., 2012b, Anagnostou et al., 2012; Stewart et al., 2016). Crosses are additional measurements from several other species of wild collected deep-sea stony corals as reported by McCulloch et al (2012b). The "×" symbols are from the symbiont-containing (zooxanthellate) temperate stony coral *Cladocora caespitosa* (Trotter et al., 2011). The fit to our cultured *B. elegans* data is more precise than existing fits to either (**b**) symbiont-free (azooxanthellate) deep-sea corals ($\delta^{11}B_{skeletal} = 0.779 \times \delta^{11}B_{borate} + 14.23$), and (**c**) to *C. caespitosa* ($\delta^{11}B_{skeletal} = 0.855 \times \delta^{11}B_{borate} + 10.32$). The slopes of these fits are statistically similar across different types of coral. Therefore, there may be a general sensitivity of skeletal $\delta^{11}B$ to borate $\delta^{11}B$ in cold-water and temperate corals. If this is the case, then our culture experiments represent one of the most precise estimates of this calibration slope to date. With respect to *B. elegans*, deep-sea corals are offset to higher skeletal $\delta^{11}B$ while *C. caespitosa* is offset lower. It is typical for symbiont-bearing corals to have lower mean skeletal $\delta^{11}B$ than azooxanthellate corals. All confidence intervals shown here at the 95% level of confidence.

SUPPLEMENTARY MATERIAL 2: GEOCHEMICAL MODEL OF CORAL BIOMINERALIZATION

Relevant details of the steady-state equilibrium model are provided here to explain our approach and results. A more detailed treatment of the model, its application to other paleoclimate problems, and its application to other marine calcifiers will be discussed in future work.

Aquatic chemistry of the calcifying fluid. The coral skeleton grows from a calcifying microenvironment that is modeled as a single box called the calcifying fluid. Evidence for physical exchange between seawater and the calcifying fluid comes from both dye uptake and isotope labeling experiments (Tambutte et al., 2012; Gagnon et al., 2012). The calcifying fluid is therefore modeled as a solution derived from seawater. In this study, the chemical reactions that are most relevant to acid-base chemistry and boron systematics are listed below (Reactions 1-4). These dissolved species are assumed to be at equilibrium and the corresponding equilibrium expressions are also listed.

$$(1) \qquad \mathrm{CO_{2(aq)} + H_2O \overset{K1}{\rightleftharpoons} HCO_3^- + H^+} \qquad K_1' = \frac{[\mathrm{HCO_3^-}][\mathrm{H^+}]}{[\mathrm{CO_{2(aq)}}]}$$

$$(2) \qquad \mathrm{HCO_3^- \overset{K2}{\rightleftharpoons} CO_3^{2-} + H^+} \qquad K_2' = \frac{[\mathrm{CO_3^{2-}}][\mathrm{H^+}]}{[\mathrm{HCO_3^-}]}$$

$$(3) \qquad \mathrm{B(OH)_3 + H_2O \overset{KB}{\rightleftharpoons} B(OH)_4^- + H^+} \qquad K_B' = \frac{[\mathrm{B(OH)_4^-}][\mathrm{H^+}]}{[\mathrm{B(OH)_3}]}$$

$$(4) \qquad \mathrm{H_2O \overset{Kw}{\rightleftharpoons} H^+ + OH^-} \qquad K_w' = [\mathrm{H^+}][\mathrm{OH^-}]$$

The prime designates stoichiometric seawater equilibrium constants with a seawater reference state, which are therefore functions of salinity in addition to temperature and pressure. Constants were calculated for T = 10.95 C, salinity = 28.45, and 1 atmosphere of pressure (surface ocean), which matches the cold-water coral culture conditions. For K_1' and K_2' we use Mehrbach et al (1973) as re-fit by Dickson & Millero (1987); for K_w' we use Millero (1995); and for K_B' we use Dickson (1990). We validated our equilibrium carbonate system solver using a subset of surface ocean GLODAP bottle data where more than two carbonate system parameters were measured simultaneously. For this dataset, the specified equilibrium constants and our carbonate system solver can use just two parameters to accurately predict other carbonate system measurements from the same sample. All constants are on the Seawater pH Scale. Model pH is converted from the Seawater pH scale to the Total

pH Scale before comparison with experimental results,

$$[\mathrm{H^+}]_{\mathrm{Total}} = [\mathrm{H^+}]_{\mathrm{Seawater}} \frac{1 + S_T/K_S^*}{1 + S_T/K_S^* + F_T/K_F^*} \quad , \tag{5}$$

where S_T, F_T, K_S^*, and K_F^* correspond to the total sulfate concentration, total fluoride concentration, bisulfate equilibrium constant, and hydrogen fluoride equilibrium constants, respectively. At the culture conditions of T = 10.95 C and salinity = 28.45, $[\mathrm{H^+}]_{\mathrm{Total}} = [\mathrm{H^+}]_{\mathrm{Seawater}} \times 0.982$ or $\mathrm{pH_{Total}} = \mathrm{pH_{SWS}} + 0.01$, which is a minor correction.

Reactions 2-4 equilibrate rapidly, however the kinetics of Reaction 1 could result in disequilibrium on timescales relevant for biomineralization. The kinetics of Reaction 1 will not directly impact boron isotopes. Kinetic effects are most relevant for isotopes systems other than those considered this study, like $\delta^{18}\mathrm{O}$, where Reaction 1 acts as a bottle neck during isotopic exchange between two large reservoirs (McConnaughey, 1989; Chen et al., 2018). Furthermore, the indirect impacts of disequilibrium in Reaction 1, which could result in a partial decoupling of $\mathrm{CO_{2(aq)}}$ from DIC, would likely only result in minor pH offsets from our equilibrium results and could also manifest as a slower apparent diffusion rate for $\mathrm{CO_{2(aq)}}$. As these are not expected to change the main patterns or conclusions of our study, we assume chemical equilibrium here and will consider the impact of kinetics on boron in future work.

If the above reactions are simultaneously in equilibrium then the system has 3 degrees of freedom. In other words, it takes three independent pieces of information to constrain the concentration of all species. For example, the system can be completely described if the values of the three following conservative properties are know: total dissolved inorganic carbon (DIC), total dissolved boron ($\mathrm{B_T}$), and alkalinity (ALK).

$$\mathrm{DIC} = [\mathrm{CO_{2(aq)}}] + [\mathrm{HCO_3^-}] + [\mathrm{CO_3^{2-}}] \tag{6}$$

$$\mathrm{B_T} = [\mathrm{B(OH)_3}] + [\mathrm{B(OH)_4^-}] \tag{7}$$

$$\mathrm{ALK} = [\mathrm{HCO_3^-}] + 2[\mathrm{CO_3^{2-}}] + [\mathrm{B(OH)_4^-}] + [\mathrm{OH^-}] - [\mathrm{H^+}] \tag{8}$$

Note, three degrees of freedom means that there are insufficient data to infer pH_{CF} from just $\delta^{11}\mathrm{B}$ and B/Ca in a single coral, because this represents just two independent pieces of information. However, this system can be solved with skeletal data across a range of conditions if there are generalizable physiological rules that govern how coral respond to seawater chemistry, an approach that we use in this study. Alternatively, a single assumption about the value of one degree of freedom can reduce the dimensionality of the system. These sorts of assumptions, usually that $\mathrm{B_T}$ of the calcifying fluid is equal to seawater $\mathrm{B_T}$, are implicit in several previous approaches.

Mole fraction expressions for the relative abundance of each major species can be derived from the above mass conservation equations and equilibrium expressions. These mole fraction relationships help simplify subsequent equations and are conveniently a function

of pH.

$$\chi_o \equiv \frac{[\mathrm{CO_{2(aq)}}]}{\mathrm{DIC}} = \frac{[\mathrm{H^+}]^2}{[\mathrm{H^+}]^2 + K_1'[\mathrm{H^+}] + K_1'K_2'} \tag{9}$$

$$\chi_1 \equiv \frac{[\mathrm{HCO_3^-}]}{\mathrm{DIC}} = \frac{K_1[\mathrm{H^+}]}{[\mathrm{H^+}]^2 + K_1'[\mathrm{H^+}] + K_1'K_2'} \tag{10}$$

$$\chi_2 \equiv \frac{[\mathrm{CO_3^{2-}}]}{\mathrm{DIC}} = \frac{K_1K_2}{[\mathrm{H^+}]^2 + K_1'[\mathrm{H^+}] + K_1'K_2'} \tag{11}$$

$$\chi_B \equiv \frac{[\mathrm{B(OH)_3}]}{\mathrm{B_T}} = \frac{[\mathrm{H^+}]}{[\mathrm{H^+}] + K_B'} \tag{12}$$

Boron isotopes and boron coprecipitation. There is a large equilibrium isotope fractionation between $\mathrm{B(OH)_3}$ (boric acid) and $\mathrm{B(OH)_4^-}$ (borate ion).

$$\alpha_{B3-B4} = \frac{\left(^{11}\mathrm{B}/^{10}\mathrm{B}\right)_{\mathrm{B(OH)_3}}}{\left(^{11}\mathrm{B}/^{10}\mathrm{B}\right)_{\mathrm{B(OH)_4^-}}} = 1.0272 \text{ (Klochko et al., 2006)} \tag{13}$$

When this fractionation is coupled to pH dependent shifts in relative speciation (χ_B; Equation 12) and subject to closed system mass balance,

$$^{11}A_T = \chi_B \ {}^{11}A_{B3} + (1 - \chi_B) \ {}^{11}A_{B4} \tag{14}$$

then the boron isotope ratio of both boric acid and the borate ion also shift with solution pH, as has been reviewed exhaustively elsewhere (for example, Hemming and Hanson, 1992; Branson, 2018). Note that abundances, where $^{11}A_T = {}^{11}B_T/(^{11}B_T + {}^{10}B_T)$, can be converted to ratios, where $^{11}R_T = (^{11}B_T/(^{10}B_T)$,

$$^{11}A = \frac{^{11}R}{^{11}R + 1} \quad . \tag{15}$$

Using Equations 13 and 14 it is possible to calculate the boron isotope ratio of both boron species as a function of pH for seawater if the isotope ratio of total dissolved boron is known. This is done numerically using a zero finding routine rather than algebraically through simplifying assumptions. Inorganic aragonite mineral growth experiments show that coprecipitated boron matches the boron isotope ratio of the borate ion without fractionation and without the growth rate effects that characterize calcite (Farmer et al., 2019). This is consistent with evidence that aragonite preferentially selects the borate ion during co-precipitaiton (Noireaux et al., 2015). The model therefore assumes that skeletal boron has the same isotope ratio as calcifying fluid $\mathrm{B(OH)_4^-}$.

Isotope ratios are reported in per mil notation referenced to NIST SRM 951 ($^{11}B/^{10}B = 4.04362$),

$$\delta^{11}\mathrm{B}_x = 1000 \left(\frac{^{11}R_x}{^{11}R_{SRM951}} - 1 \right) \quad . \tag{16}$$

Total dissolved boron of modern seawater has a value of 39.61 ‰ on this scale (Foster, 2010).

The B/Ca data from inorganic aragonite coprecipiation experiments do not show the strong kinetic effects of calcite and are consistent with a few different forms of the partition coefficient. Here we use the two forms of the partition coefficient that best fit the inorganic precipitation data from Holcomb et al., (2016). For example,

$$(\mathrm{B/Ca})_{sk} = 0.085 + 2.88\frac{\mathrm{B_T}}{\mathrm{DIC}} \tag{17}$$

In this equation B/Ca is in units of mmol/mol while the units of B_T and DIC must match, for example μmol kg^{-1}. The implementation of the model is modular and can accommodate different transfer functions. For example, changing this partition coefficient to

$$(\mathrm{B/Ca})_{sk} = C + m\frac{[\mathrm{B(OH)_4^-}]}{\sqrt{[{\mathrm{CO_3}}^{2-}]}} \tag{18}$$
$$C = 0.041 \pm 0.024$$
$$m = 0.0604 \pm 0.0044$$

only shifts the modeled B/Ca to slightly higher values, but does not alter the main trends nor does it change the conclusions of our paper. In this equation B/Ca is in units of mmol/mol while $[\mathrm{B(OH)_4^-}]$ and $[{\mathrm{CO_3}}^{2-}]$ are in units of μmol kg^{-1}. The fitting terms C and m are shown with 2σ standard errors, as reported in the original publication.

Biomineralization fluxes. Calcifying fluid chemistry is modified through a host of physiological and geochemical processes. While a large number of processes could be considered, we attempted to find the simplest general model that could reproduce our data and make useful predictions. We then show that it is unnecessary to know specific fluxes. Instead we show that skeletal chemistry is primarily controlled by just three low dimension parameters. To interpret the significance of these parameters and explain the structure of the model, we start by defining individual fluxes. The model includes fluxes due to skeletal precipitation (P) in moles $CaCO_3$ m^{-2} sec^{-1}; seawater exchange (k) in sec^{-1}, where k is just the inverse of the calcifying fluid residence time; and diffusion of the nonpolar species CO_2 and $B(OH)_3$. One major difference between this and other models is the consideration of boric acid diffusion. Diffusion D of a species across the cell membrane is put in terms of a piston velocity in units of m sec^{-1}. This piston velocity simply represents the diffusion coefficient in m^2 sec^{-1} multiplied by the cell membrane thickness. The piston velocity D is specific to $CO_{2(aq)}$ diffusion. To allow for differences between CO_2 and $B(OH)_3$ diffusion we define the parameter β, such that the piston velocity for $B(OH)_3$ is $D_B = D/\beta$.

The model also includes active ion pumping by the coral organism. To keep the components of the model as general as possible this flux is treated as alkalinity pumping (F) in units of 2x mole equivalents m^{-2} sec^{-1}. This is equivalent to $Ca^{2+} - 2H^+$ exchange, and there is evidence that pumps of this type participate in coral biomineralization (Zoccola et al., 2004). Other stoichiometries are equivalent from the perspective of the main governing

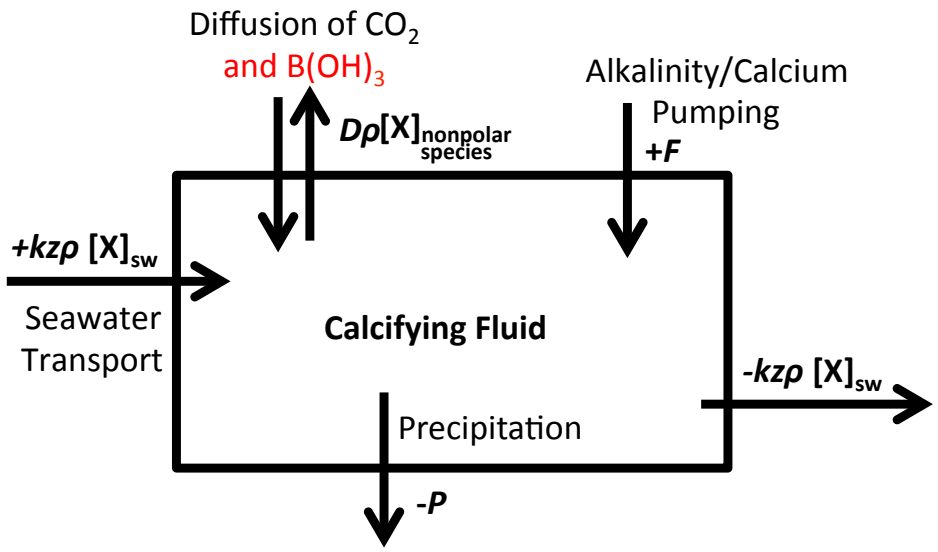

FIGURE 1. **Model diagram with fluxes.** All fluxes have all been converted into the units of moles m^{-2} sec^{-1} for this figure, using the density of seawater (ρ) in kg m^3 and the volume to surface area ratio of the calcifying space (z) in m^3/m^2. The term z is also equivalent to the idealized height in m of the calcifying fluid if it were a box with the same surface area to volume ratio.

equations of the model, including $2Na^+ - 2H^+$ or $2K^+ - 2H^+$ exchange. The only impact of these different modes of ion pumping would be on $[Ca^{2+}]$ (see below) but this term is not necessary to determine the B/Ca and boron isotope composition of the skeleton in our model.

The impact of the combined fluxes on calcifying fluid composition leads to the following system of differential equations:

$$\begin{aligned}(19)\qquad \frac{d\mathrm{DIC}}{dt} = {} & k\mathrm{DIC}_{sw} - k\mathrm{DIC} && \text{seawater exchange}\\ & + \frac{D}{z}[\mathrm{CO_2}]_{ext} - \frac{D}{z}\chi_0\mathrm{DIC} && \mathrm{CO_2}\text{ diffusion}\\ & - \frac{P}{z\rho} && \mathrm{CaCO_3}\text{ precipitation}\end{aligned}$$

$$\begin{aligned}(20)\qquad \frac{d\mathrm{ALK}}{dt} = {} & k\mathrm{ALK}_{sw} - k\mathrm{ALK} && \text{seawater exchange}\\ & - \frac{2P}{z\rho} && \mathrm{CaCO_3}\text{ precipitation}\\ & + \frac{2F}{z\rho} && \text{alkalinity pumping}\end{aligned}$$

$$\begin{aligned}(21)\qquad \frac{d[\mathrm{B_T}]}{dt} = {} & k[\mathrm{B_T}]_{sw} - k[\mathrm{B_T}] && \text{seawater exchange}\\ & + \frac{D}{z}\frac{1}{\beta}[\mathrm{B(OH)_3}]_{ext} - \frac{D}{z}\frac{1}{\beta}\chi_B[\mathrm{B_T}] && \mathrm{B(OH)_3}\text{ diffusion}\\ & - \left(\frac{\mathrm{B}}{\mathrm{Ca}}\right)_{sk}\frac{P}{z\rho} && \text{boron coprecipitation}\end{aligned}$$

$$\begin{aligned}(22)\qquad \frac{d[^{11}\mathrm{B_T}]}{dt} = {} & k[\mathrm{B_T}]_{sw}{}^{11}A_{Tsw} - k[\mathrm{B_T}]^{11}A_T && \text{seawater exchange}\\ & + \frac{D}{z}\frac{1}{\beta}[\mathrm{B(OH)_3}]_{ext}{}^{11}A_{B3sw} - \frac{D}{z}\frac{1}{\beta}\chi_B[\mathrm{B_T}]^{11}A_{B3} && \mathrm{B(OH)_3}\text{ diffusion}\\ & - \left(\frac{\mathrm{B}}{\mathrm{Ca}}\right)_{sk}\frac{P}{z\rho}{}^{11}A_{B4} && \text{boron coprecipitation}\end{aligned}$$

Variables without subscripts refer to the calcifying fluid. We assume that isotopic fractionation of boric acid during diffusion is negligible. Steady-state solutions of the above differential equations can be simplified so that they are a function of a small number of

low dimension dynamic variables.

$$0 = \mathrm{DIC}_{sw} - \mathrm{DIC} + \frac{D}{kz}[\mathrm{CO_2}]_{ext} - \frac{D}{kz}\chi_0 \mathrm{DIC} - \frac{P}{kz\rho} \tag{23}$$

$$0 = \mathrm{ALK}_{sw} - \mathrm{ALK} + (\gamma - 1)\frac{P}{kz\rho} \tag{24}$$

$$0 = [\mathrm{B_T}]_{sw} - [\mathrm{B_T}] + \frac{D}{kz}\frac{1}{\beta}[\mathrm{B(OH)_3}]_{ext} - \frac{D}{kz}\frac{1}{\beta}\chi_B[\mathrm{B_T}] - \left(\frac{\mathrm{B}}{\mathrm{Ca}}\right)_{sk}\frac{P}{kz\rho} \tag{25}$$

$$\begin{aligned} 0 = {} & [\mathrm{B_T}]_{sw}\,{}^{11}A_{Tsw} - [\mathrm{B_T}]\,{}^{11}A_T + \frac{D}{kz}\frac{1}{\beta}[\mathrm{B(OH)_3}]_{ext}\,{}^{11}A_{B3sw} \\ & - \frac{D}{kz}\frac{1}{\beta}\chi_B[\mathrm{B_T}]\,{}^{11}A_{B3} - \left(\frac{\mathrm{B}}{\mathrm{Ca}}\right)_{sk}\frac{P}{kz\rho}\,{}^{11}A_{B4} \end{aligned} \tag{26}$$

We introduce the term $\gamma = F/P$ to simplify the above equations. This non-dimensional parameter has physiological significance because it represents the amount of active ion pumping relative to the amount of precipitation, therefore it is a measure of calcification efficiency. The variable $P/kz\rho$ represents the balance between precipitation and seawater exchange. It is in concentration units (mol kg^{-1}) and equals the steady state draw down of alkalinity or calcium, modulated by γ, and it therefore acts as an indicator for the extent of Rayleigh fractionation. The non dimensional variable D/kz represents the balance between diffusion and seawater exchange.

The following variables are all set to match the composition of the culture solution for a specific coral: DIC_{sw}, ALK_{sw}, ${}^{11}A_{Tsw}$, ${}^{11}A_{B3sw}$,$[\mathrm{CO_2}]_{ext}$, and $[\mathrm{B(OH)_3}]_{ext}$. Setting $[\mathrm{CO_2}]_{ext}$ and $[\mathrm{B(OH)_3}]_{ext}$ to match the surrounding seawater means that the D values represent a diffusive path to seawater. Changing this assumption for $[\mathrm{CO_2}]_{ext}$ and setting it to various estimates of intracellular $\mathrm{CO_2}$ concentrations does not affect the pattern or main conclusions of our paper. The assumption that boric acid can be in diffusive contact with seawater, even if the corresponding diffusion coefficient is small relative to other processes, is reasonable given that few cellular processes consume or produce boron species and that these processes are small compared to the amount of boron in seawater.

When solved simultaneously, the system of Equations 23-26, together with the previous equations, have only three degrees of freedom. This means that $P/kz\rho$ and D/kz together with one other piece of information are sufficient to completely describe calcifying fluid chemistry and skeletal geochemistry. Imagine, for example that we have a measurement pH_{CF} or that we would like to test an assumption about calcifying fluid pH. In this case there are only two degrees of freedom left, and all possible valid model states with that pH can be represented on a 2-dimensional plot of $P/kz\rho$ vs. D/kz. In this space, different regions of the plot correspond to different classes of models. For example, a model that assumed seawater transport is negligible and that the ions for calcification are transported primarily through pumping corresponds to the upper right quadrant, where both $P/kz\rho$ and D/kz are large. By exploring this whole space, our model is agnostic and unbiased

with respect to questions like the relative importance of seawater exchange, diffusion, precipitation, and ion pumping.

Numerical approach. Calcifying fluid chemistry is determined from pH_{CF}, $P/kz\rho$ and D/kz using the following procedure. The mole fractions χ_B, χ_0, and χ_2, which are only functions of pH, are calculated from pH_{CF}. The steady-state DIC of the calcifying fluid is then calculated using Equation 23. Combined with χ_2 this yields the $[CO_3^{2-}]$. The steady-state B_T of the calcifying fluid is then calculated from Equation 25 and the partition coefficient described in either Equations 18 or 17. The value of B_T together with χ_B provides values for $[B(OH)_3]$ and $[B(OH)_4^-]$. There is now sufficient information to calculate ALK using the definition of alkalinity, and with ALK, all other unknown chemical parameters. Boron isotopes are calculated using Equation 26, together with equilibrium fractionation and mass balance.

Inverting the parameters of cold-water coral biomineralization. The forward modeling approach described above yields the calcifying fluid chemistry and skeletal chemistry for a set of assumptions about pH_{CF}, $P/kz\rho$ and D/kz and a corresponding set of of culture conditions. However, we are interested in the relationships between seawater conditions and pH_{CF}, $P/kz\rho$ and D/kz that can explain our geochemical data. These "rules" of coral calcification may have predictive power and can provide mechanistic insight. To uncover these rules we invert the B/Ca and $\delta^{11}B$ data from one of our three experiments and then test if these rules have the power to predict our remaining, independent and chemically distinct coral results.

In practice, pH_{CF} and mean D/kz are primarily set by $\delta^{11}B$; the $\delta^{11}B$-DIC effect determines the DIC dependence of D/kz; and $P/kz\rho$ is primarily controlled by the mean value of B/Ca. Several combinations of parameters can explain our constant pH data. However, once physically impossible fluxes are excluded and only actively calcifying states are considered, the parameters cluster in a small region of model space. Physically impossible fluxes are those that lead to negative concentrations. States corresponding to undersaturation imply dissolution, and while they may be valid, we do not consider them here because they do not lead to skeletal growth and therefore do not preserve boron signals. We first present one simple set of rules (Scenario A) that can reproduce the constant pH dataset and which also accurately predict the other experiments. Using this example as a starting point, we then show that there is an even more concise set of rules with a correspondingly set of simple physiological interpretations that can also explain our data (Scenario B, presented in the main paper). With regards to B/Ca, this simpler set of rules even predicts our data better.

The procedure for inverting the model using only data from the constant pH experiment (**Scenario A**) is described below. Quantities with a bar over them represent reference

values that are constant, in this case they correspond to ambient conditions.

$$\begin{cases} \text{1. Postulate that } D/kz\rho \text{ is a linear function of } \mathrm{DIC_{SW}}: \\ \qquad D/kz\rho = \overline{D/kz\rho} + slope\left(\mathrm{DIC_{SW}} - \overline{\mathrm{DIC_{SW}}}\right) \\ \text{2. Adjust } \mathrm{pH}_{CF} \text{ and } \overline{D/kz\rho} \text{ to fit model to mean skeletal } \delta^{11}B. \\ \text{3. Adjust } slope \text{ to fit } \delta^{11}B \text{ vs. } \mathrm{DIC_{SW}} \text{ relationship.} \\ \text{4. Assume that } P/kz\rho \text{ is constant :} \\ \qquad \text{adjust } P/kz\rho \text{ to fit model to mean skeletal B/Ca.} \\ \text{5. Iterate to adjust for interactions between previous steps.} \end{cases}$$

The resulting model parameters from fitting data from the constant pH experiment:

$$\text{Constant } P/kz\rho\text{, } \textbf{Scenario A}\text{: } \begin{cases} \mathrm{pH}_{CF} = 9.0 \\ \mathrm{D/kz} = 1.5 + 500\ \frac{\mathrm{kg}}{\mathrm{mol}}\left(\mathrm{DIC}_{sw} - 2500 \times 10^{-6}\ \frac{\mathrm{mol}}{\mathrm{kg}}\right) \\ P/kz\rho = 5 \times 10^{-4}\ \frac{\mathrm{mol}}{\mathrm{kg}} \end{cases}$$

Comparisons between model results and experimental data are shown in Supplemental Figures 2-4. Note that δ^{11}B is sensitive to pH, which explains the δ^{11}B paleo pH proxy even though none of the three model parameters are explicit functions of seawater pH, nor was the model tuned to match experiments where pH varies. The B/Ca vs. DIC effect also emerges from the model without fitting or tuning. The model B/Ca vs $\mathrm{DIC_{SW}}$ slope is similar to the data. The model also predicts higher scatter within the constant DIC experiment, a pattern that is present in the data. These patterns remain if the form of the partition coefficient is changed. While individual B/Ca data points are at the edge or within the error envelope of model predictions, which is promising, it is also clear that the mean of two trends are different. It is not surprising that there may be differences in the mean values of partition coefficients between inorganic minerals and biominerals at the 10-20 % level. This offset is eliminated in the simpler set of rules (Scenario B) described below.

Individual Physiological Fluxes. The low dimensional parameters $P/kz\rho$ and D/kz, together with pH_{CF} are the most relevant quantities for understanding skeletal geochemistry, and their values have mechanistic implications even if they represent ratios. However, with independent knowledge of one flux, the implied values for all other fluxes can be calculated to further explore the significance of these empirical biomineralization parameters. For this reason, we add an aragonite mineral growth law to the model,

$$P = k_{rate}(\Omega - 1)^n \tag{27}$$
$$\Omega = [\mathrm{Ca^{2+}}][\mathrm{{CO_3}^{2-}}]/\mathrm{K'_{sp}} \quad .$$

The rate constant ($k = 7.58 \times 10^{-12}$ mol m^{-2} sec^{-1}) and the order of the reaction ($n = 0.786$) were interpolated to the temperature of our coral culture experiments using the inorganic aragonite mineral growth data of Burton & Walter (1987), which were conducted at multiple temperatures. We use the solubility constant (K'_{sp}) of aragonite in seawater from Mucci (1983). The mineral growth rate law requires knowledge of calcifying

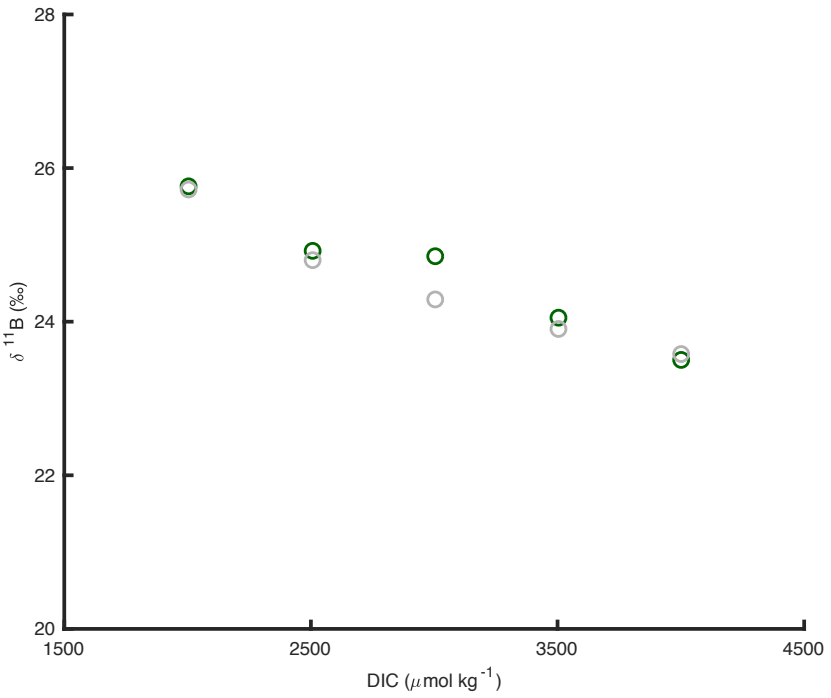

FIGURE 2. **Model is fit to measured skeletal δ^{11}B for constant pH experiment (Scenario A-Constant $P/kz\rho$).** The fit between modeled (gray) and measured (green) data is optimized by adjusting pH_{CF} and D/kz. pH_{CF} is set to a constant value of 9.0 in this scenario regardless of seawater conditions. Only $D/kz\rho$ is allowed to vary with DIC_{SW}. Note that few processes other than boric acid diffusion can result in a systematic decrease in δ^{11}B. Furthermore, the other options, like prescribing a drop in calcifying fluid pH as a function of seawater DIC, do not have general predictive power and cannot therefore predict the pH dependence of δ^{11}B seen in our other independent experiments.

fluid $[\mathrm{Ca}^{2+}]$ even if the overall model does not. The $[\mathrm{Ca}^{2+}]$ is governed by the following differential equation,

$$\begin{aligned} \frac{d[\mathrm{Ca}^{2+}]}{dt} = \; & k[\mathrm{Ca}^{2+}]_{sw} - k[\mathrm{Ca}^{2+}] && \text{seawater exchange} \\ & - \frac{P}{z\rho} && \mathrm{CaCO_3}\text{ precipitation} \\ & + f\frac{F}{z\rho} && \text{alkalinity pumping} \quad . \end{aligned} \tag{28}$$

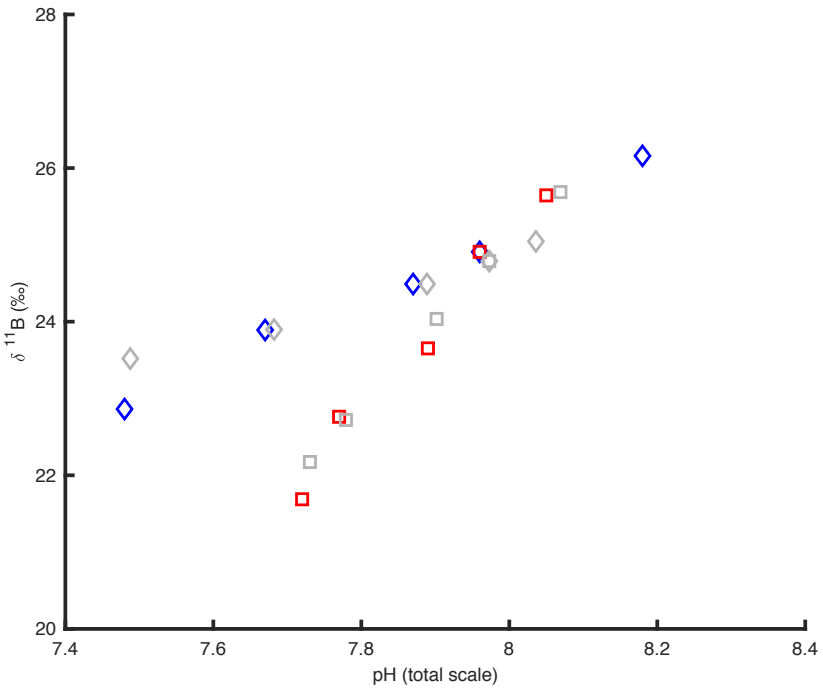

FIGURE 3. **Comparison of model predictions compared with skeletal δ^{11}B for constant DIC and constant $[CO_3^{2-}]$ experiments shows good match (Scenario A-Constant $P/kz\rho$).** The correspondence between modeled (gray) and measured (colored) data is not the result of directly fitting these data. Symbols as described in previous plots. Note the x-offset between calculated and measure pH for many of the data points. This is because the model calculates seawater pH from the average culture seawater DIC and average culture seawater ALK, while the measured data are plotted using the measured average culture seawater pH for each condition. Data follow a similar trend even if there is a minor offset.

A choice must be made about the stoichiometry of ion pumping. The term f is the fraction of alkalinity pumping that is done through Ca^{2+}-$2H^+$ exchange. In the current model we assume all alkalinity pumping occurs through this process ($f = 1$). This assumption does not impact boron and boron isotopes. However, changes in f can impact metal-calcium ratios in the skeleton because partition coefficients for these systems are sensitive to changes in $[Ca^{2+}]$. At steady-state, and with this assumption,

$$0 = [Ca^{2+}]_{sw} - [Ca^{2+}] + f(\gamma - 1)\frac{P}{kz\rho} \quad . \tag{29}$$

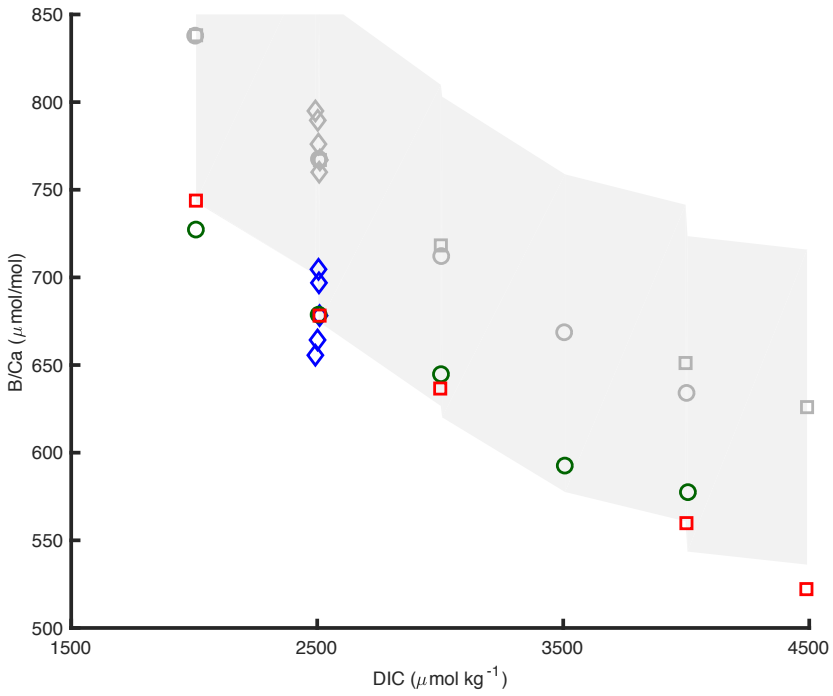

FIGURE 4. **Comparison between modeled and measured skeletal B/Ca shows correct trend and significant offset (Scenario A-Constant $P/kz\rho$).** Model results indicated with gray symbols. Shaded region indicates 2σ confidence interval for modeled B/Ca propagated from uncertainty in the partition coefficient as indicated in the inorganic mineral growth experiments of Holcomb et al. (2016). Measured skeletal composition indicated with colored markers. Symbols and colors as in previous plots.

Comparing this with Equation 24 shows that steady-state ALK and $[Ca^{2+}]$ are linearly dependent when $f = 1$ so the calcium equations neither add nor require new information in this case.

If $P/kz\rho$ is held constant, like in Scenario A, then this implies systematic changes to both seawater transport and diffusion as seawater DIC changes. Organisms do change membrane characteristics in response to environmental cues, a notable example is found in phytoplankton that can change membrane fluidity as a function of temperature. However, it is not clear why changes to diffusion would necessarily behave in this systematic way for coral. Instead, we think it is more likely that D is maintained at an approximately constant value regardless of environmental conditions. As we show below, this assumption

that D is constant leads to similarly well-matched δ^{11}B results as well as an improved match between modeled and measured B/Ca.

Procedure for inverting model using only data from the constant pH experiment while assuming that diffusion (D) is constant (**Scenario B**):

$$
\left\{
\begin{array}{l}
\text{1. Postulate that } D/kz\rho \text{ is a linear function of } \mathrm{DIC_{SW}}: \\
\qquad\qquad D/kz\rho = \overline{D/kz\rho} + \mathit{slope}\left(\mathrm{DIC_{SW}} - \overline{\mathrm{DIC_{SW}}}\right) \\
\text{2. Adjust } \mathrm{pH}_{CF} \text{ and } \overline{D/kz\rho} \text{ to fit model to mean skeletal } \delta^{11}B. \\
\text{3. Adjust } \mathit{slope} \text{ to fit } \delta^{11}B \text{ vs. } \mathrm{DIC_{SW}} \text{ relationship.} \\
\text{4. Assume that } D \text{ is constant :} \\
\qquad\qquad \text{adjust } D \text{ to fit model to mean skeletal B/Ca.}
\end{array}
\right. \tag{30}
$$

These rules can be translated into physiological terms. Within the model, coral hold the pH of the calcifying fluid constant regardless of environmental conditions. The diffusion coefficient for boric acid and dissolved carbon dioxide does not change with environmental conditions either. However, seawater exchange systematically decreases with seawater DIC. This last rule is an implication of the DIC dependence of D/kz together with a constant D. The values of pH_{CF} and D, together with the DIC dependence of either kz or D/kz are fit to the constant pH data set:

$$
\text{Constant } D, \textbf{ Scenario B}\text{: } \left\{
\begin{array}{l}
\mathrm{pH}_{CF} = 8.95 \\
\mathrm{D/kz} = 1.1 + 500\ \frac{\mathrm{kg}}{\mathrm{mol}}\ \left(\mathrm{DIC}_{sw} - 2500 \times 10^{-6}\ \frac{\mathrm{mol}}{\mathrm{kg}}\right) \\
D = 1.5 \times 10^{-10}
\end{array}
\right.
$$

This simple set of rules and values are sufficient to explain the δ^{11}B and B/Ca data from the other independent experiments as shown in Figures 5-8. Both of the B/Ca partition coefficients (Equations 18-17) result in a close correspondence between modeled and measured data. The value of D used in the model (order 10^{-10}) is lower than measurements of boric acid diffusion across the membrane of plant cells (order 10^{-6}), by several orders of magnitude (Dordas & Brown, 2000). This may reflect that our D represents diffusion between the calcifying fluid and seawater, a path through the coral tissue which presumably requires diffusion across several membranes. Furthermore, $\beta = D_{CO2}/D_{BOH3}$ is kept at 1 in our model for simplicity. However, $[\mathrm{CO_2}]_{\mathrm{aq}}$ diffuses through membranes faster than boric acid by several orders of magnitude, implying that a more realistic value of β should be larger than 1. A sensitivity test where β is varied, shows that this parameter affects mean skeletal B/Ca, and to a far lesser extent, the slope of the B/Ca vs. DIC relationship, but it does not affect δ^{11}B. Changes to β also lead to different calcifying fluid saturation states (Ω) and different efficiencies γ, but the trends discussed in this paper are not changed. It is possible that consideration of carbonate system kinetics would narrow the gap between measured and modeled values of β. This is because kinetics would tend to slow $[\mathrm{CO_2}]_{\mathrm{aq}}$ hydration/hydroxylation which would likely decreases the "effective β", bringing it closer to 1. This kinetic analysis awaits future work. In the meantime, our basic sensitivity test shows that our main conclusions are robust to shifts in β.

Implications of the Biomineralization Rules. Because the model provides a detailed view of calcifying fluid chemistry, it is possible to explore the implications of our rules for questions beyond δ^{11}B and B/Ca. The rules in both Scenarios A & B result in similar trends for calcifying fluid chemistry. The DIC of the calcifying fluid increases with DIC_{SW} because of seawater exchange (Fig. 9). Because χ_2 is only a function of pH, increasing DIC at constant pH_{CF} implies that the $[\mathrm{CO}_3^{2-}]$ also increases with DIC_{SW}. By extension, the saturation state of the calcifying fluid (Ω) also increase with DIC_{SW} (Fig. 10). However, lines of constant pH and lines of constant Ω have only slightly different slopes in plots of ALK vs. DIC. This means that large changes in DIC translate into relatively smaller changes in Ω when pH_{CF} is constant. Seawater DIC impacts calcifying fluid Ω but the effect is most noticeable when changes in DIC_{SW} are very large. Acting through the inorganic mineral growth rate law, increasing Ω with DIC_{SW} means that precipitation rate (P) also increases with DIC_{SW} (Fig. 11). All of these trends are robust to large changes in model parameters. While the trends hold, changes in model parameters like pH_{CF} and D (Scenario B) or pH_{CF} and $P/kz\rho$ (Scenario A) do change the mean value of parameters like calcifying fluid DIC, Ω, and P. For Scenario A & B, typical Ω values range near 10-20, consistent with recent direct measurements of calcifying fluid Ω in a tropical coral (Sevilgen et al., 2019). This corresponds to precipitation rates for Scenario B between $4 \times 10^{-11} < P < 8 \times 10^{-11}$ mol m^{-2} sec^{-1}.

For Scenario B, varying D/kz with constant D implies a systematic decease in seawater transport kz with DIC_{SW} (Fig. 13). Together with increasing P, as a function of DIC_{SW}, this decreasing kz means that $P/kz\rho$ increases with DIC_{SW} (Fig. 14), which should have implications for those skeletal metal/calcium that are driven by Rayleigh effects. This topic will be discussed in future publications. In contrast, our δ^{11}B and B/Ca results are similar between Scenario A, where $P/kz\rho$ is held constant and Scenario B, where $P/kz\rho$ increase with DIC_{SW}. Thus our boron results are robust to different extents of Rayleigh or "reservoir" processes. This lack of sensitivity is consistent with the fact that boron coprecipitation fluxes are small compared with the amount of boron in seawater and that the B/Ca partition coefficients used for aragonite do not depend on $[\mathrm{Ca}^{2+}]$.

Calcifying fluid efficiency ($\gamma = F/P$) indicates the amount of ion pumping (F) that a coral must do compared to the amount of precipitation (P) that the coral achieves from this pumping. Since P is a function of DIC_{SW}, the sensitivity of γ to different seawater conditions is largely set by F, as discussed in the main text. Pumping increases with ocean acidification (OA). We simulate ocean acidification through changes in seawater DIC at constant ALK that yield a range of pCO_2 between 310 and 1060 ppm. This recipe for OA is equivalent to carbon dioxide uptake, which does not change ALK. As P does not change much with OA, but F increase dramatically, γ also increases with OA (Figs. 15-16). Our model says that that coral must expend more energy on pumping per unit of skeletal growth as ocean acidification gets worse. The model also implies that this sensitivity to OA is related to organism-scale energy needs rather than direct chemical control of precipitation. Indeed, P increases with OA in our model, albeit at a shallow slope. This

predicted trend in skeletal growth with DIC_{SW}, regardless of other seawater conditions, is present in our experimental data (see Supplemental Information Part A for plots of skeletal mass vs. DIC_{SW}). The fact that we see this effect across a large range of DIC but OA experiments on the same species of coral do not see much a strong effect in skeletal growth is likely because the range of DIC in the OA experiment is much smaller.

Like Ω and P, changes in model parameters like pH_{CF} and D (Scenario B) or pH_{CF} and $P/kz\rho$ (Scenario A) change the mean value of γ. However, trends in γ as a function of seawater chemistry are robust to large changes in these model parameters. Higher mean γ values just tend to decrease the relative importance of the OA effect. High values of γ imply inefficient calcification and are associated with values of Ω that are much larger than recent direct measurements in tropical coral (Sevilgen et al., 2019). For this reason we think that the low values of γ corresponding to Scenario A & B are more realistic than higher γ values. It is also possible to achieve values of γ that are less than 1, but this tends to cause B/Ca to diverge from measured B/Ca at the 10-20 % level. Such accuracy offsets are within the propagated error of inorganic partition coefficient. Again, trends in γ with OA and other aspects of seawater chemistry are robust to these changes in mean γ.

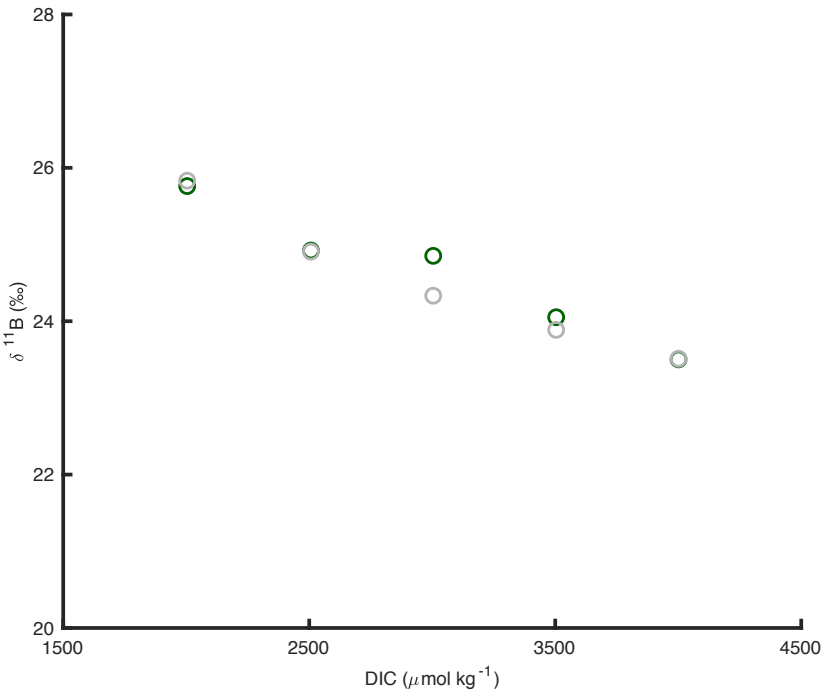

FIGURE 5. **Model is fit to measured skeletal δ^{11}B for constant pH experiment (Scenario B–Constant *D*).** The fit between modeled (gray) and measured (green) data is optimized by adjusting pH_{CF} and D/kz. pH_{CF} is set to a constant value of 8.95 regardless of seawater conditions. Only $D/kz\rho$ is allowed to vary with DIC_{SW} and does so following a linear relationship.

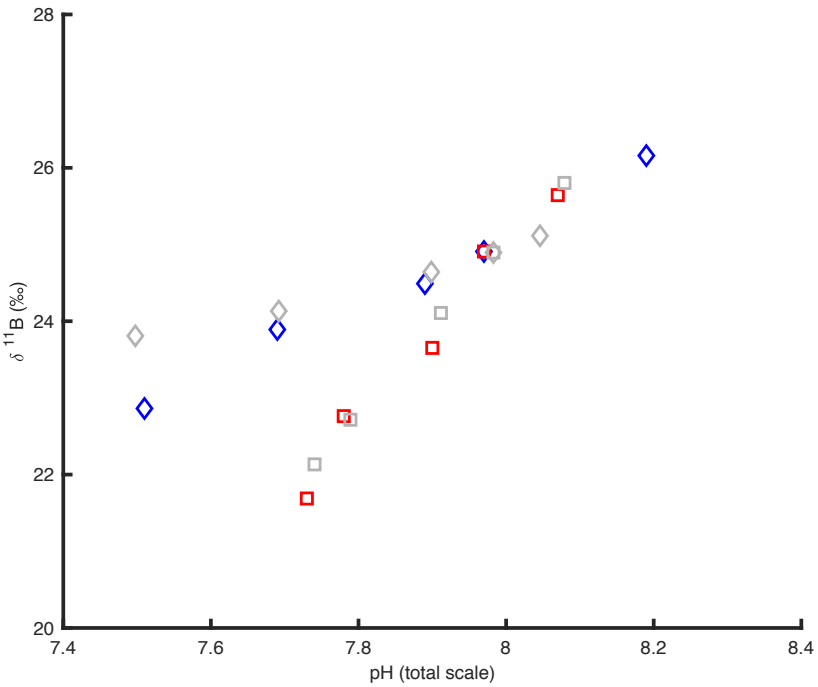

FIGURE 6. **Comparison of model predictions with measured skeletal δ^{11}B for constant DIC and constant $[CO_3^{2-}]$ experiments shows good match (Scenario B–Constant *D*).** The correspondence between modeled (gray) and measured (colored) data is not the result of directly fitting these data. This relationship between δ^{11}B and pH is instead an emergent property due to boric acid diffusion. Symbols as described in previous plots. This is the same comparison as shown in the main paper Fig. 3c.

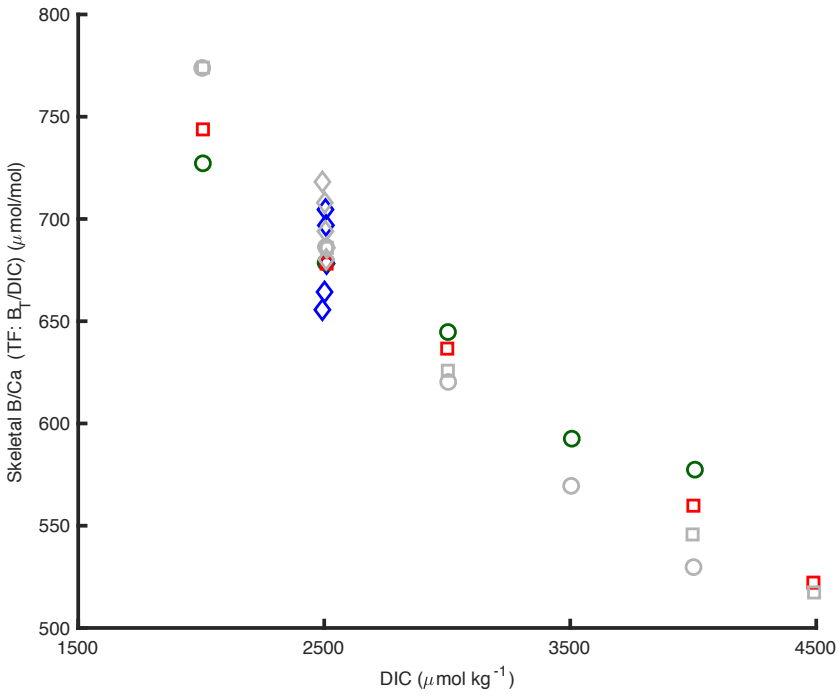

FIGURE 7. **Comparison between modeled and measured skeletal B/Ca shows good match when the partition coefficient is put in terms of DIC (Scenario B–Constant *D*).** As noted on the y-axis, the B/Ca partition coefficient, or transfer function(TF), for this plot is in terms of B_T and DIC (Equation 17). Model results indicated with grey symbols. Measured skeletal composition indicated with colored markers. Symbols and colors as in previous plots. The relationship between B/Ca and DIC_{SW} is not the result of a direct model fit, but is instead an emergent property due to boric acid diffusion. This is the same type of comparison as shown in the main paper Fig. 3d.

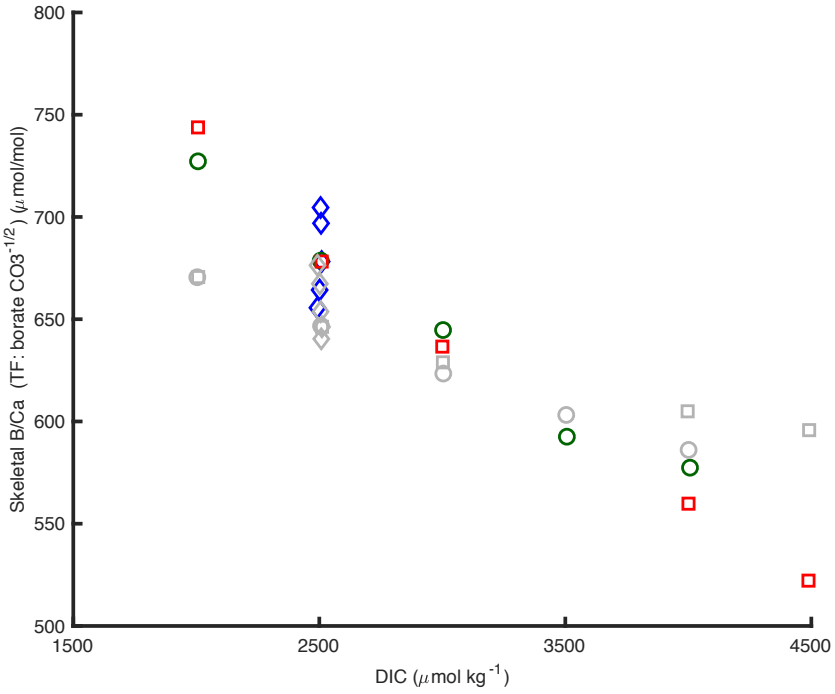

FIGURE 8. **Comparison between modeled and measured skeletal B/Ca with the alternative partition function shows good match except at high DIC (Scenario B–Constant *D*).** As noted on the y-axis, the B/Ca partition coefficient, or transfer function(TF), for this plot is in terms of borate ion and the square root of the carbonate ion (Equation 18). Model results indicated with gray symbols. Measured skeletal composition indicated with colored markers. Symbols and colors as in previous plots. The relationship between B/Ca and DIC_{SW} is not the result of a direct model fit, but is instead an emergent property due to boric acid diffusion.

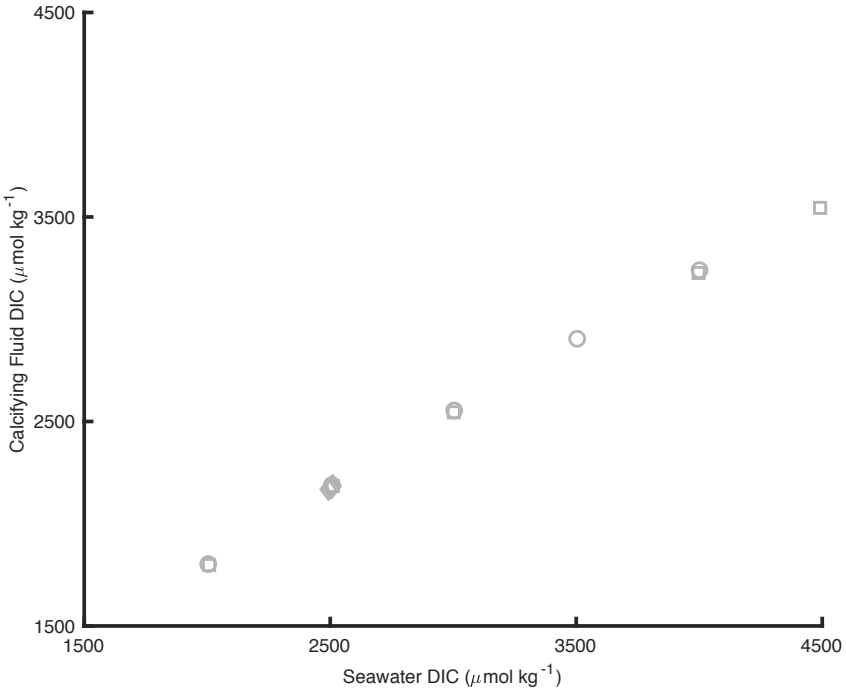

FIGURE 9. **Relationship between modeled calcifying fluid DIC and seawater DIC (Scenario B-Constant *D*).** The correlation between calcifying fluid DIC and seawater DIC is driven by exchange between seawater and the calcifying fluid. Because calcifying fluid DIC is lower than seawater DIC (below a 1:1 line), this seawater exchange results in a net inward flux of DIC, which helps to supply some of the materials necessary for skeletal growth. Symbols correspond to experimental conditions as in previous plots. As in other plots, modeled data is gray. No experimental data shown for this plot because we do not have direct measurements of calcifying fluid chemistry.

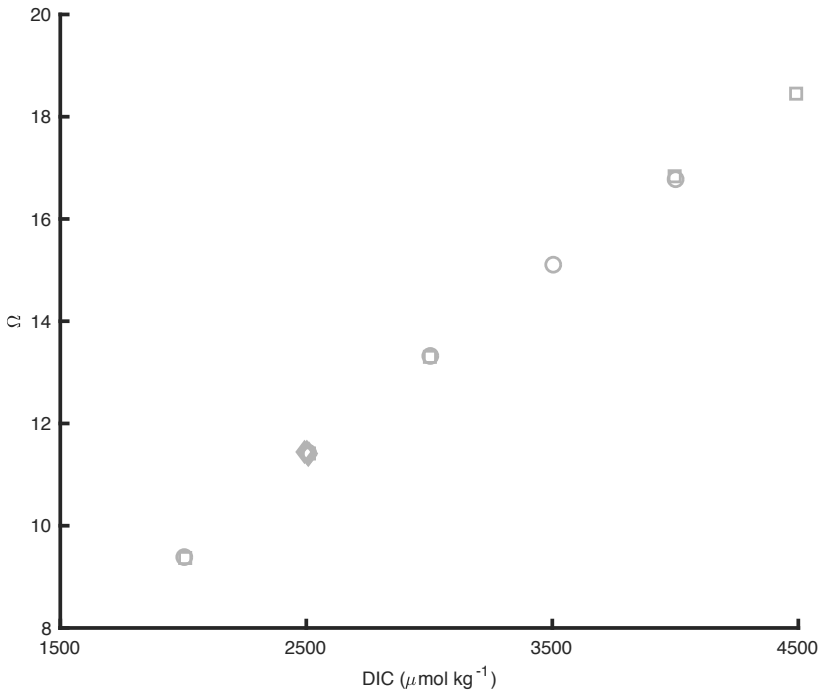

FIGURE 10. **Relationship between modeled calcifying fluid saturation state (Ω) and seawater DIC (Scenario B-Constant D).** Saturation state rises from roughly 10 to 20 as DIC_{SW} increases. At constant pH, $[\mathrm{CO}_3^{2-}]$ is a linear function of DIC. Thus, as DIC_{CF} rises with DIC_{SW}, $[\mathrm{CO}_3^{2-}]_{\mathrm{CF}}$ rises as well, and by extension so does the aragonite saturation state Ω. Symbols correspond to experimental conditions as in previous plots. As in other plots, modeled data is gray. No experimental data shown for this plot because we do not have direct measurements of calcifying fluid chemistry.

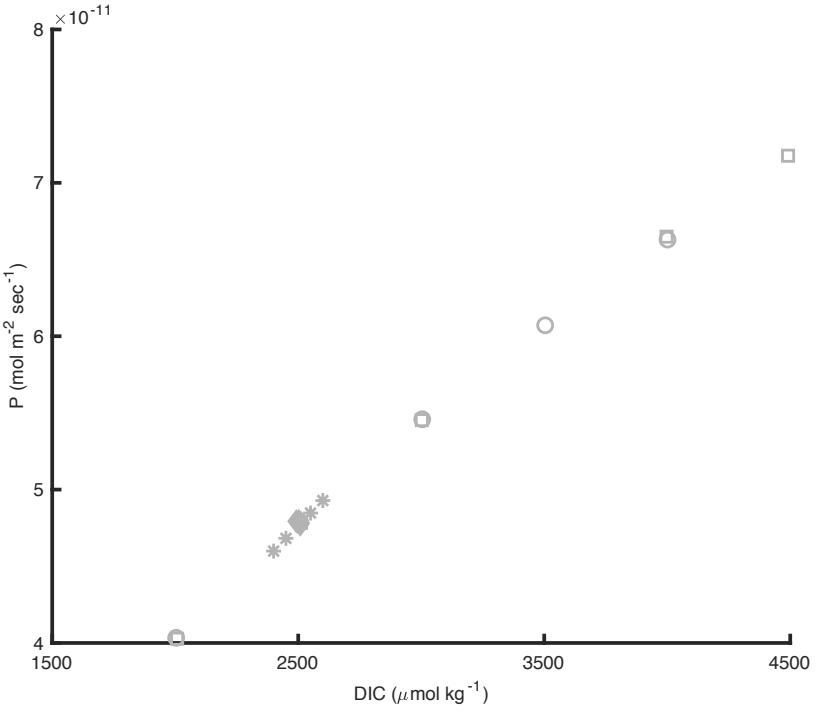

FIGURE 11. **Relationship between modeled precipitation rate (P) and seawater DIC (Scenario B-Constant D).** Like Ω in the previous plot, precipitation rate increases with DIC_{SW}, as expected given that the inorganic mineral growth rate law is a function of Ω. In this plot, model results from a simulated ocean acidification (OA) experiment are also plotted as $*$ symbols. Precipitation rates for modeled OA conditions follow the same relationship with DIC_{SW} as other experiments. Seawater DIC increases as a result of OA with the low DIC $*$ corresponding to a pCO_2 of 310 ppm and the high DIC $*$ corresponding to a pCO_2 of 1060 ppm. Note that this implies a slight increase in P with acidification. Additional symbols correspond to experimental conditions as in previous plots: Constant DIC ($\diamond$); Constant carbonate ($\square$); Constant pH ($\circ$). As in other plots, modeled data is gray. No experimental data shown for this plot because we do not have direct measurements of instantaneous precipitation rate that can be directly compared with the model.

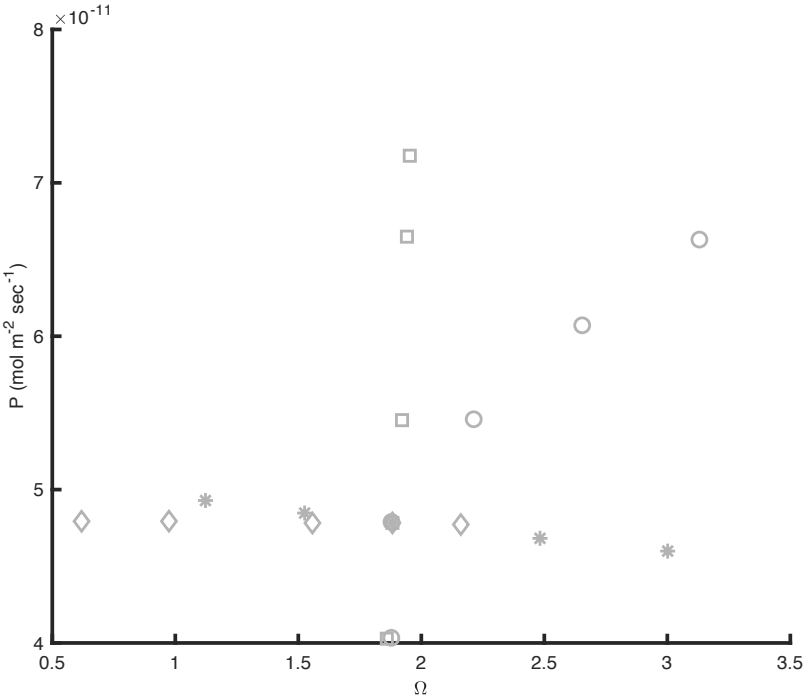

FIGURE 12. **Relationship between modeled precipitation rate (P) and seawater saturation state (Scenario B-Constant D).** Same data as the previous figure, just plotted against the saturation state of seawater (Ω). This plot shows how precipitation rates for modeled OA conditions ($*$ symbols) are a weak function of seawater Ω and are even predicted to increase slightly with undersaturation. Seawater saturation state decreases as a result of OA, with the high Ω OA data points corresponding to a pCO_2 of 310 ppm and the low Ω data points corresponding to a pCO_2 of 1060 ppm. Additional symbols correspond to experimental conditions as in previous plots: Constant DIC ($\diamond$); Constant carbonate ($\square$); Constant pH ($\circ$). As in other plots, modeled data is gray. No experimental data shown for this plot because we do not have direct measurements of instantaneous precipitation rate that can be directly compared with the model. Note that the strong apparent effects for the constant pH experiment ($\circ$) and constant carbonate ion experiment ($\square$) are actually driven by large changes in culture water DIC, as shown in the previous plot.

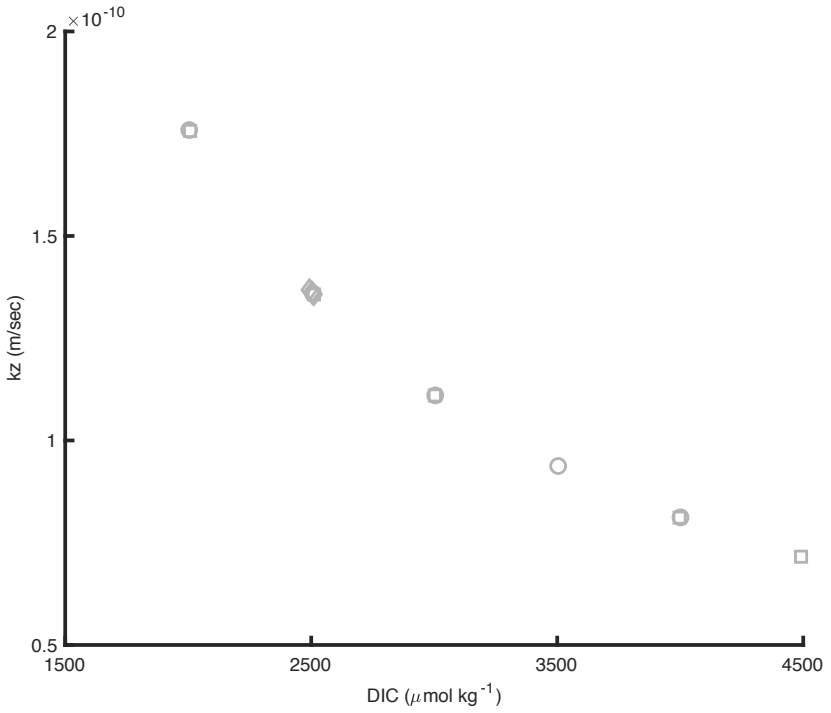

FIGURE 13. **Relationship between modeled seawater flux (kz) and seawater DIC (Scenario B-Constant D).** This relationship is one of the postulated rules. The slope of this relationship together with the assumption that D is constant is what sets the sensitivity of skeletal δ^{11}B to DIC_{SW}. The seawater exchange flux is written as a piston velocity in units m sec^{-1}. While the choice of D impacts the value of kz, for this model run (Scenario B) the implied residence time is is on the order of 10s of minutes to an hour. This is consistent with Gagnon et al. (2013), if the idealized calcifying space height (z) is on the order of 1 μm. Symbols correspond to experimental conditions as in previous plots. As in other plots, modeled data is gray. No experimental data shown for this plot because this is a model parameter.

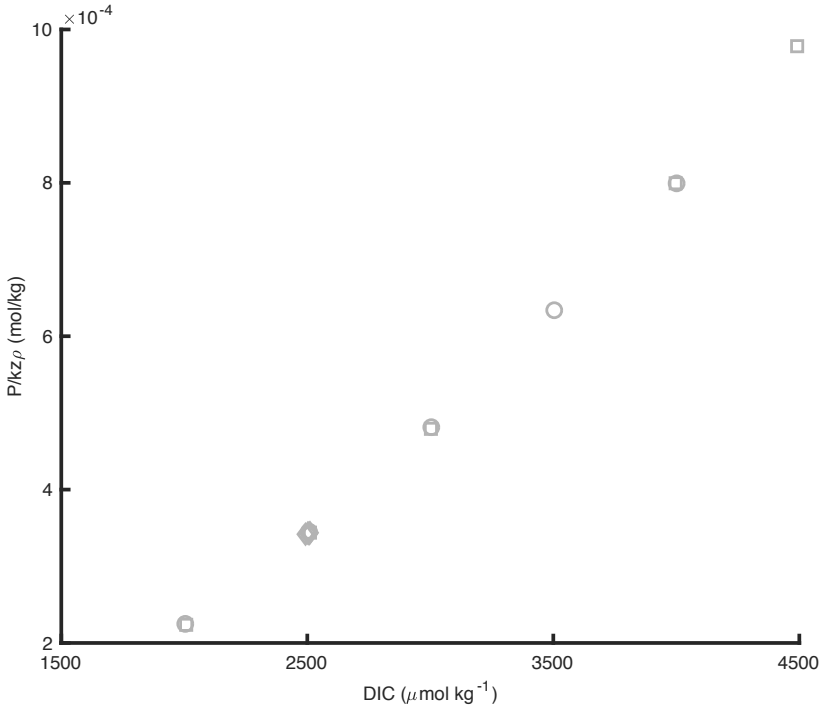

FIGURE 14. **Relationship between the model parameter $P/kz\rho$ and seawater DIC (Scenario B-Constant D).** The model parameter ($P/kz\rho$) has concentration units and indicates the steady-state drawdown of ALK in the calcifying fluid due to precipitation. On its own, this relationship implies larger extents of Rayleigh or "closed system" behavior at higher DIC_{SW}. However, the pumping flux (F) and the fraction of pumping (f) that involves calcium ions will modulate this predicted Rayleigh effect. $P/kz\rho$ increases with DIC_{sw} due to the postulated decrease in kz, discussed in the previous plot, together with the positive correlation between P and DIC_{sw}, discussed above. Symbols correspond to experimental conditions as in previous plots. As in other plots, modeled data is gray. No experimental data shown for this plot because this is a model parameter.

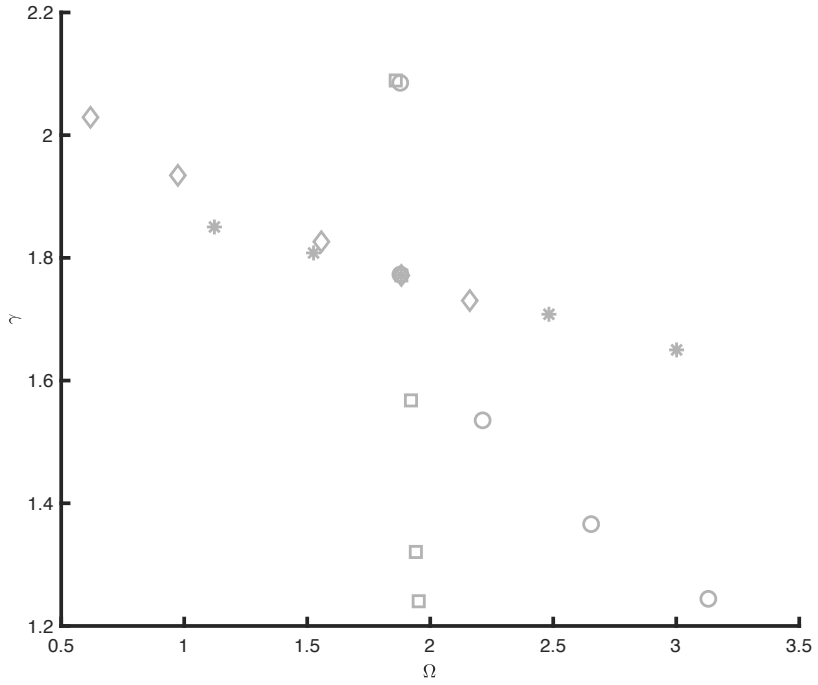

FIGURE 15. **Relationship between the modeled calcification efficiency ($\gamma = F/P$) and seawater saturation state (Ω) (Scenario B-Constant *D*).** In this figure, model results from a simulated ocean acidification (OA) experiment are plotted as $*$ symbols. Low Ω values correspond to less efficient calcification ($\gamma = F/P$ increases at low Ω). Recall that seawater saturation state decreases as a result of OA, with the high Ω $*$ corresponding to a pCO_2 of 310 ppm and the low Ω $*$ corresponding to a pCO_2 of 1060 ppm. Additional symbols correspond to experimental conditions as in previous plots: Constant DIC ($\diamond$); Constant carbonate ($\square$); Constant pH ($\circ$). As in other plots, modeled data is gray. Note that the strong apparent effects for the constant pH experiment ($\circ$) and constant carbonate ion experiment ($\square$) are actually driven by large changes in culture water DIC, as shown in the next plot.

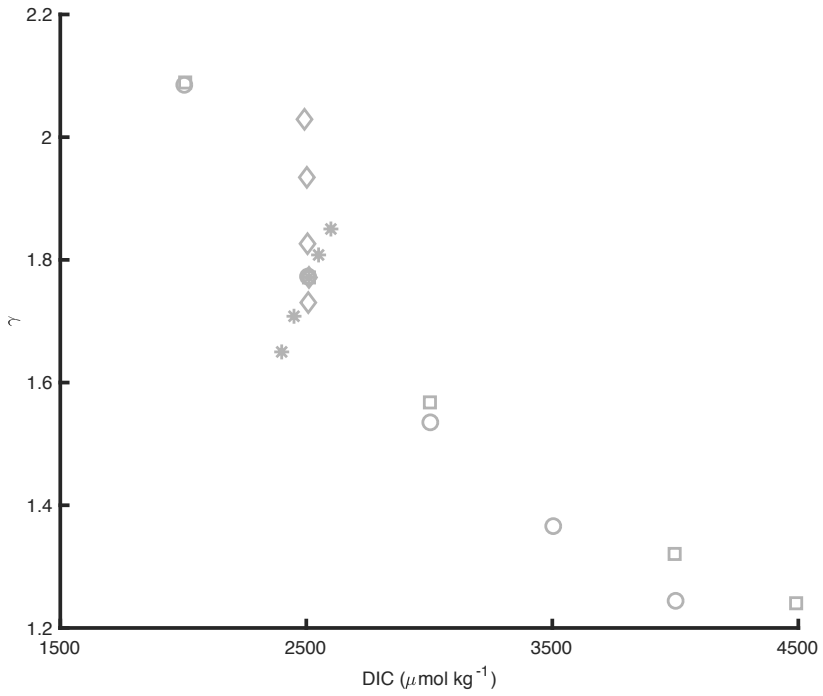

FIGURE 16. **Relationship between the modeled calcification efficiency ($\gamma = F/P$) and seawater DIC shows inefficiency is exacerbated as DIC grows during OA (Scenario B-Constant D).** Model results from a simulated ocean acidification (OA) experiment are plotted as $*$ symbols. Seawater DIC increases as a result of OA with the low DIC $*$ corresponding to a pCO_2 of 310 ppm and the high DIC $*$ corresponding to a pCO_2 of 1060 ppm. These higher DIC values correspond to less efficient calcification ($\gamma = F/P$ increases with DIC). Compared with the constant pH experiment ($\circ$) and constant carbonate ion experiment ($\square$), the sensitivity of $\gamma = F/P$ to DIC is stronger and of the opposite slope during ocean acidification (steep positive slope for $*$ symbols). The constant DIC experiment ($\diamond$) is a vertical line by definition. Additional symbols correspond to experimental conditions as in previous plots: Constant DIC ($\diamond$); Constant carbonate ($\square$); Constant pH ($\circ$). As in other plots, modeled data is gray.

Supplemental References

Branson, O. Boron Incorporation into Marine CaCO3 Boron Incorporation into Marine CaCO3. In: Marschall H., Foster G. (eds) Boron Isotopes. Advances in Isotope Geochemistry. Springer (2018).

Burton & Walter. Relative precipitation rates of aragonite and Mg calcite from seawater: Temperature or carbonate ion control? *Geology* **15**, 111-114 (1987).

Dickson. Thermodynamics of the dissociation of boric acid in synthetic seawater from 273.15 to 318.15 K. *Deep-sea Res.* **37**, 755-766 (1990).

Dickson & Millero. A comparison of the equilibrium constants for the dissociation of carbonic acid in seawater media. *Deep-Sea Res.* **34**, 1733-1743 (1987).

Dordas, C. & Brown, P.H., Permeability of boric acid across lipid bilayers and factors affecting it. *The Journal of membrane biology* **175**, 95-105 (2000).

Farmer, J. et al. Boric acid and borate incorporation in inorganic calcite inferred from B/Ca, boron isotopes and surface kinetic modeling. *Geochim. Cosmochim. Acta* **244**, 229-247 (2019).

Foster, G, Pogge von Strandmann, P.A.E., Rae, J.W.B. Boron and magnesium isotopic composition of seawater. *Geochem. Geophys. Geosyst.* **11**, Q08015 (2010).

Gagnon, A., Adkins, J, & Erez, J. Seawater transport during coral biomineralization. *Earth Planet. Sci. Lett.* **329-330**, 150-161 (2012).

Hemming, N., and Hanson, G. Boron isotopic composition and concentration in modern marine carbonates. *Geochim. Cosmochim. Acta* **56**, 537-543 (1992).

Holcomb et al., Factors affecting B/Ca ratios in synthetic aragonite. *Chem. Geol.* **437**, 67-76 (2016).

Klochko et al. Experimental measurement of boron isotope fractionation in seawater. *Earth and Planet. Sci. Lett.* **248**, 276-285 (2006).

McConnaughey T. 13C and 18O isotopic disequilibrium in biological carbonates. 2. In vitro simulation of kinetic isotope effects. *Geochim. Cosmochim. Acta* **53**, 151?162 (1989).

Mehrbach et al. MEASUREMENT OF THE APPARENT DISSOCIATION CONSTANTS OF CARBONIC ACID IN SEAWATER AT ATMOSPHERIC PRESSURE. *Limnol. Oceanogr.* **18**, 897-907 (1973).

Millero Thermodynamics of the carbon dioxide system in the oceans. *Geochim. Cosmochim. Acta* **59**, 661-677 (1995)

Mucci. The solubility of calcite and aragonite in seawater at various salinities, temperatures, and one atmosphere total pressure. *Am. Journal. Sci.* **283**, 780-799 (1983).

Sevilgen et al., Full in vivo characterization of carbonate chemistry at the site of calcification in corals. *Science Advances* **5**, eaau7447 (2019).

Tambutte, E., et al. Calcein labelling and electrophysiology: insights on coral tissue permeability and calcification. *Proc. R. Soc. B.* **279**, 19-27 (2012).

Zoccola, D., Tambutte, E. & Kulhanek, E. Molecular cloning and localization of a PMCA P-type calcium ATPase from the coral Stylophora pistillata. *Biochim. Biophys. Acta* **1663**, 117?126 (2004).